



**University of
Nottingham**

UK | CHINA | MALAYSIA

Computational modelling of electrostatic interactions between colloidal patchy particles

Małgorzata Stankiewicz

Student Number: 20300496

Thesis submitted to the University of Nottingham
for the degree of Master of Research

**Supervised by Prof. Elena Besley (95%) &
Prof. Anthony J. Stace (5%)**

School of Chemistry
University of Nottingham

30th September 2021

Acknowledgements

I wish to express my gratitude to everyone for their kind words and understanding throughout this work.

Foremost, I would like to thank my principal supervisor Professor Elena Besley for invaluable support and help throughout the whole year of this research, dedicated time, patience and understanding, sharing her expertise and passion and giving numerous priceless life advice, and also bringing nature into our group meetings.

I would like to sincerely thank my secondary supervisor Professor Anthony Stace for irreplaceable help with structuring my thesis, valuable comments that saved me from many mistakes and shortcomings, kindness and support throughout the research.

I would like to thank the Fraunhofer Institute for Applied Polymer Research IAP for the opportunity to collaborate with Prof. Dr. rer. nat. Alexander Böker and Dr. Dmitry Grigoriev as a part of this project. I am very grateful for introducing me to the ongoing research from the experimental side and giving me ideas.

I express my profound gratitude to Dr Joshua Baptiste for his endless willingness to help throughout the whole time, answering each of my questions and explaining numerous scientific phenomenons with exceptional engagement, sharing his enormous knowledge of MATLAB, encouraging and believing in me in every day of my journey. Thank you, Josh, for giving me all the pieces of advice, sharing ideas and showing me shortcuts that saved me from doing much time-consuming work.

I would like to extend my gratitude to Dr Steve Skowron for his constructive comments, sharing valuable sources and tools, patience, engagement and guidance throughout this project.

I would like to thank Josh, Abi, and Ben, for becoming my second home, thank you for introducing me closely to English culture and thank you for looking

out for me.

I would also like to thank the whole Compchem group for making me feel welcome and thank you for the joyful environment at the university and the always pleasant time we spent together after work.

Thank you and I miss you all!

I would not be able to complete this work without my loving parents, who are also my best friends. Thank you for encouraging me and always being there for me.

Abstract

Controlled self-organisation of patchy colloidal particles depends mainly on weak forces - reversible electrostatic interactions. Developments in the modelling of patchy particles can help understanding more in-depth the influence of self-assembly systems and predict desired structure formation.

The report presents the implementation of non-uniform charge distribution with the ability to modelling desired size patches. A range of trends is displayed to demonstrate the reliability and robustness of the model. Following this, a recreation of results, analysis and prediction for experimental work published in 2020 by Mehr et al.[1] is presented.

As an additional extension of this project, atomic-scale small systems were explored by applying charged dielectric polarisable particles model. The accuracy of the classical model was investigated, and the ability to approximate neutral atoms and ions was examined.

Nomenclature

Abbreviations/Acronyms

CCSD(T)	Coupled-Cluster with single-double and perturbative triple
DFT	Density-functional theory
FITC	fluorescein isothiocyanate
FMM	Fast Multipole Method
MF	melamine formaldehyde
MP2	second-order Møller-Plesset perturbation theory
PDMS	polydimethylsiloxane
PEI	polyethyleneimine
PMVEMA	poly(methyl vinyl ether-alt-maleic acid)

Symbols

a	radius
d	distance from the two expected values
d_c	chord length
h	centre-to-centre separation
k	dielectric constant (relative permittivity)
s	surface-to-surface separation
t	central angle
q	free-charge distribution
q_g	total charge
α	atomic polarisability
ε	absolute permittivity
ε_r	relative permittivity
ε_0	vacuum permittivity
Φ	electric potential

Symbols

σ	total surface charge density
σ_g	Gaussian surface charge density
σ_s	uniform charge density
Γ	denomination of a particles surface in the many-body formalism
D	electrical displacement
E	electric field
\mathcal{E}	total energy
F	electrostatic force
L	centre-to-centre separation between two atoms/ions
N	umber of molecules per unit of volume
P	polarization density
\mathbb{R}^3	three-dimensional space
U	total energy
U_e	potential energy
$U(L)$	polarisation portion of the total interaction energy
$\hat{\mathbf{n}}$	unit vector perpendicular to a point on a sphere's surface
v	standard deviation
μ	expected value
$\boldsymbol{\mu}$	vector of the expected values
Ω_M	many-body system of non-overlapping dielectric spheres
P	factor that determines the "flatness" of the top of Gaussian

Contents

Acknowledgements	i
Abstract	iv
Nomenclature	v
1 Introduction to self-assembly of patchy particles	1
2 Theoretical background to modelling electrostatic interactions	8
2.1 Polarisation in dielectrics	8
2.2 Two-body polarisable electrostatic solution	10
2.3 Many-body polarisable electrostatic solution	13
3 Analytical representation of the localised surface charge; modelling a patch	17
3.1 Higher-order Gaussian distribution	18
3.1.1 Testing higher-order Gaussian distribution of charge . . .	24
3.2 Numerical validations	28
3.3 Modelling a patch	38
4 Computational modelling of oppositely charged inverse bi-patchy particles	40
4.1 Comparison of charge distribution methods	40
5 Conclusions and Future Work	49
Bibliography	51
Appendices	55
A Supporting results	55
B Atomic scale modelling using dielectric spheres	58

List of Figures

1.1	The classification of anisotropic particles divided into two groups: a) surface anisotropy and b) particle shape anisotropy. Anisotropic molecules can be further subdivided by combining surface and shape anisotropy - reproduced from reference[2].	2
1.2	a) Reaction schemes of the production of the oppositely charged patches on the surface of an MF particle made of prelabeled PMVEMA and PEI with Rhodamine 6G and FITC, respectively. b) SFM height image of a PMVEMA patch. c) SEM image of a PEI patch. d) SEM image of a bipatchy MF particle. e,f) fluorescence and the overlaid microscope images of bipatchy MF particles with patches made of PMVEMA (red) and PEI (green). Scale bars:1 μm - reproduced from reference[1]	4
1.3	Particles connections formed via random interactions between patchy and non-patchy surfaces of MF particles, together with % of experimentally observed connections in the aggregates formed by MF particles. The fraction of PEI patch interactions is larger than the fraction of PMVEMA interactions due to the higher yield of PEI patches - reproduced from reference[1]	6
2.1	Geometric representation of the many-body system Ω_M with radius \mathbf{a}_i and centred at x_i , dielectric constant k_i , in a homogeneous medium of dielectric constant k_0 [3].	14

3.1 σ as function of the ratio v/a , where $q_1 = q_2 = +1e$. For $k_m = k_p = 1$ and $a = 1$ nm. Patches with normal Gaussian distribution ($P = 1$, yellow), and higher-order Gaussian distribution ($P = 2$, blue) and ($P = 5$, purple). 21

3.2 Visual representations of the surface charge density on a non-polarisable sphere $a = 1$ nm where $q = -1e$ 22

3.3 Interaction energy as a function of the ratio v/a_1 . $P = 1$ (yellow solid line), $P = 2$ (blue solid line), $P = 5$ (purple solid line), where $q_1 = +1e$ and $q_2 = -1e$. For $a_1 = a_2 = 1$ nm at $s = 1000$ nm. The dashed line represents the interaction between two point-charges $q_1 = +1e$ and $q_2 = -1e$ at $s = 1000$ nm. . . . 23

3.4 Higher-order Gaussian distribution when using equation (3.7), where $(\mu_x; \mu_y)$ is the centre. 24

3.5 Visual representations of two point charges: (a) when the charge density is uniform, it can be approximated to be a point charge at the centre of the sphere (on the particle's surface), (b) Gaussian distribution - a patch of charge placed on the particle's surface. Red point represents a point charge with $q_1 = +1e$ and the blue dot is a point charge with $q_2 = -1e$ 25

3.6 Interaction energy as a function of surface-to-surface separation s for uniform method (the potential energy equation (3.8) - orange solid, model's results - orange dots); Gaussian method (the potential energy equation (3.8) - purple solid, model's results - purple dots), the Gaussian patches on a_1 and a_2 are facing the same direction, $P = 5$ and $v/a_1 = 0.8$; results for point charge model's results - purple circles. Position of the point charges - figure 3.5. Remaining variables: $a_1 = 1$ nm, $a_2 = 2$ nm, where $q_1 = +1e, q_2 = -1e$ for $k_m = k_p = 1$ 26

3.7 A geometric representation of two-body system. Each sphere has two oppositely charged patches with $q_1 = +1e$ (red patch) and $q_2 = -1e$ (blue patch) placed on a particle's surface. The second sphere moves away from the first sphere with surface-to-surface separation distance s 27

3.8 Interaction energy plots between two bipatchy particles (figure 3.7) as a function of surface-to-surface separation s for $P = 1$ (purple), $P = 2$ (blue), $P = 3$ (red), $P = 4$ (black), $P = 5$ (cyan) using equation (3.7); $k_m = k_p = 1$, $a_1 = a_2 = 1$ nm. 28

3.9 Electrostatic force as a function of surface-to-surface separation s between two bipatchy particles (figure 3.7). Patch geometry is defined by $v = 0.8$ and $P = 5$ using equation (3.7). For $a_1 = 1$ nm, $k_p = 20$, $k_m = 1$ and $a_2 = 1$ nm (light blue), $a_2 = 2$ nm (dark blue), $a_2 = 3$ nm (purple). 29

3.10 Interaction energy as a function of surface-to-surface separation s between two bipatchy particles (figure 3.7). Patch geometry is defined by $v = 0.8$ and $P = 5$ using equation (3.7). For $a_1 = 1$ nm, $k_p = 20$, $k_m = 1$ and $a_2 = 1$ nm (yellow), $a_2 = 2$ nm (blue), $a_2 = 3$ nm (purple). 30

3.11 Interaction energy as a function of surface-to-surface separation s between two bipatchy particles (figure 3.7). Patch geometry is defined by $v = 0.8$ and $P = 5$ using equation (3.7). For $a_1 = a_2 = 1$ nm, $k_p = 20$, $k_m = 1$. The charge vary on a_2 : $q = +1e$ (yellow), $q = +2e$ (green), $q = +3e$ (purple). 32

3.12 Interaction energy as a function of surface-to-surface separation s between bipatchy particles. Patch geometry is defined by $v = 0.8$ and $P = 5$ using equation (3.7); red patch $q = +1e$ and blue patch $q = -1e$. For $k_p = 20$, $k_m = 1$, particles radii $a = 1$ nm. 33

- 3.13 Interaction energy as a function of surface-to-surface separation s between bipatchy particles. Patch geometry is defined by $v = 0.8$ and $P = 5$ using equation (3.7); red patch $q = +1e$ and blue patch $q = -1e$. For $k_p = 20$, $k_m = 1$; particles radii $a = 1$ nm. 34
- 3.14 Interaction energy as a function of α for the interaction between two bipatchy particles at a fixed surface-to-surface separation $s = 0.001$ nm. Patch geometry is defined by $v = 0.8$ and $P = 5$ using equation (3.7); red patch $q = +1e$ and blue patch $q = -1e$. For $k_p = 20$, $k_m = 1$, $a = 1$ nm and $a_2 = 1$ nm (yellow), $a_2 = 2$ nm (blue), $a_2 = 3$ nm (purple). 35
- 3.15 Interaction energy as a function of α for the interaction between two bipatchy particles at a fixed surface-to-surface separation $s = 0.001$ nm. For $k_p = 20$, $k_m = 1$; $a_1 = a_2 = 1$ nm. Patch geometry are defined by $v = 0.8$ and $P = 5$ using equation (3.7); $q_1 = +1e$ (red patch) and $q_2 = -1e$ (blue patch) - yellow plot; $q_1 = +1e$ (red patch) and $q_2 = -0.9e$ (blue patch) - blue plots. 36
- 3.16 Interaction energy as a function of α for the interaction between two bipatchy particles at a fixed surface-to-surface separation $s = 0.001$ nm. For $k_p = 20$, $k_m = 1$; $a_1 = a_2 = 1$ nm; $q_1 = +1e$ (red patch) and $q_2 = -1e$ (blue patch); Patches geometry: $P = 5$; all patches $v = 0.8$ (magenta); positive red patch $v = 0.8$ and negative blue patch $v = 0.7$ (cyan solid line), positive red patch $v = 0.7$ and negative blue patch $v = 0.8$ (cyan dashed line) using equation (3.7). 37
- 3.17 Visualisation of variables required for the equation (3.9) for chord length d_c 38

- 4.1 Interaction energy as a function of surface-to-surface separation s . Recreation of results from Mehr et al. (figure 5a) [1] - solid lines. Interaction between bi-patchy particles with variables set to $P = 5$ and $v/a_{1,2} = 0.27$ for PEI patch and $v/a_{1,2} = 0.28$ for PMVEMA patch (using equation (3.7)) to recreate the patch's size from the experimental results in Mehr et al.[1]. Negatively charged patch PMVEMA $q = -0.923$ fC (red colour) and positively charged patch PEI $q = +0.734$ fC (green colour). 42
- 4.2 Interaction energy as a function of surface-to-surface separation distance between particles. Recreation of results from Mehr et al. (figure 5b) - solid lines. Interaction between bi-patchy and mono-patchy particle with variables set to $P = 5$ and $v/a_{1,2} = 0.27$ for PEI patch and $v/a_{1,2} = 0.28$ for PMVEMA patch (using equation (3.7)) to recreate the patch's size from the experimental results in Mehr et al. Negatively charged patch PMVEMA $q = -0.923$ fC (red colour) and positively charged patch PEI $q = +0.734$ fC (green colour). 43
- 4.3 Interaction energy as a function of surface-to-surface separation distance between particles. Interaction between five-body system with uniformly distributed charge on each particle – recreation of results from Small by Mehr et al. (solid lines). Interaction between bi-patchy and mono-patchy particles with variables set to be $P = 5$ and $v/a_{1,2} = 0.27$ for PEI patch and $v/a_{1,2} = 0.28$ for PMVEMA patch to recreate the patch's size from the experimental results. Negatively charged patch PMVEMA $q = -0.923$ fC (red colour) and positively charged patch PEI $q = +0.734$ fC (green colour); figure b shows interaction energy as a function of surface-to-surface separation distance between particles only from the distance $s = 5.181$ μm 45

4.4	The re-orientation of a bi-patchy pair from a stable PMVEMA-PEI configuration ($\alpha = 0^\circ$) to a repulsive PEI-PEI connection ($\alpha = 180^\circ$).	46
4.5	The calculated rotational barrier (in fJ) for re-orientation of a bi-patchy pair from a repulsive PEI-PEI connection ($\alpha = 180^\circ$) to a stable PMVEMA-PEI configuration ($\alpha = 0^\circ$) at two surface-to-surface separation distances: 2 μm (black), and 4 μm (red). The particle rotates around stationary particle facing the stationary particle with PEI patch. The calculated rotational barrier (in fJ) for re-orientation of a bi-patchy pair from a repulsive PEI-PEI connection ($\alpha = 180^\circ$) to a stable PMVEMA-PEI configuration ($\alpha = 0^\circ$) at two surface-to-surface separation distances: 7.18 μm (black), and 9.18 μm (red). The rotating particle remains at fixed position.	47
5.1	Interaction energy as a function of surface-to-surface separation s for overlapping particles method (solid), and point charges using the potential energy equation 3.8 (dashed).	50
A.1	Electrostatic force as a function of surface-to-surface separation s between two bipatchy particles (figure 3.7). For $a_1 = 1$ nm, where $v = 0.8$, $P = 5$; $k_p = 20$; $k_m = 1$. The patches increase in size along with the particle's size $a_2 = 1$ nm (light blue), $v = 0.8$ and $P = 5$; $a_2 = 2$ nm (dark blue), $v = 1.6$ and $P = 5$; $a_2 = 3$ nm (purple), $v = 2.4$ and $P = 5$ using equation (3.7).	55
A.2	Interaction energy as a function of surface-to-surface separation s between two bipatchy particles (figure 3.7). For $a_1 = 1$ nm, where $v = 0.8$, $P = 5$; $k_p = 20$; $k_m = 1$. The patches increase in size along with the particle's size $a_2 = 1$ nm (yellow), $v = 0.8$ and $P = 5$; $a_2 = 2$ nm (blue), $v = 1.6$ and $P = 5$; $a_2 = 3$ nm (purple), $v = 2.4$ and $P = 5$ using equation (3.7).	56

- A.3 Interaction energy as a function of surface-to-surface separation s between two bipatchy particles (figure 3.7). For $a_1 = 1$ nm, where $v = 0.8$, $P = 5$; $k_p = 20$; $k_m = 1$. The patches increase in size along with the particle's size $a_2 = 1$ nm (yellow), $v = 0.8$ and $P = 5$; $a_2 = 2$ nm (blue), $v = 1.6$ and $P = 5$; $a_2 = 3$ nm (purple), $v = 2.4$ and $P = 5$ using equation (3.7). 57
- B.1 The polarisation portion of the interaction energy $U(L)$, in atomic units, for $\text{Al}^+ - \text{Al}^+$. The calculations are done with the CCSD(T)/aug-cc-pVTZ with no frozen core orbitals method (black), the density functional theory at the B3LYP/6-31G(d) level (yellow), MP2/6-31G* (light blue) For the rigorous classical formalism for two dielectric spheres three choices of parameters: $k_p = 3.52$, $a_1 = a_2 = 2\text{\AA}$ (green); $k_p = 154.96$, $a_1 = a_2 = 1.54\text{\AA}$ (magenta); $k_p = 1.915$, $a_1 = a_2 = 2.49\text{\AA}$ (red). 61
- B.2 The polarisation portion of the interaction energy $U(L)$, in atomic units, for $\text{Al} - \text{Al}^+$. The calculations are done with the CCSD(T)/aug-cc-pVTZ with no frozen core orbitals method (black), the density functional theory at the B3LYP/6-31G(d,p) level (yellow), MP2/6-31G* (light blue) For the rigorous classical formalism for two dielectric spheres two choices of parameters: $k_p = 3.49$, $a_{\text{Al}^+} = 2\text{\AA}$, $a_{\text{Al}} = 4.07\text{\AA}$ (dark blue); $k_p = 1.93$, $a_{\text{Al}^+} = 2.48\text{\AA}$, $a_{\text{Al}} = 5.05$ (red). 62

Chapter 1

Introduction to self-assembly of patchy particles

The presence of electrostatic interactions influences underlying physical processes that occur in the natural world and those directed in the laboratory. Electrostatic forces impact in the self-assembly of particles in nano- and microscale regimes. The self-assembly phenomenon is the result of spatially directed interparticle local electrostatic interactions and particles, so-called building blocks with diverse functionalities, shape and/or chemical composition[1, 2] that undergo the formation of structures with higher complexity[4–6]. Those interparticle interactions lead such a system to assemble in a structure with the energy in the lowest possible state. The interactions of the electrostatic nature play a substantial role in understanding the agglomeration of cosmic dust and charged ice particles in the mesosphere[7], aerosol growth in Titan’s atmosphere (Saturn’s moon)[8], and biological systems such as protein to protein interactions[9] or DNA-protein binding[10]. Controlled self-organization of particles has progressed the production of materials with desired properties, such as optical, electrical or magnetic[11–15]. This method, which occurs by control of interparticle interactions, has leveraged the research intensity in a range of niche areas but is still an experimentally tricky process to achieve.

The properties of the material containing anisotropic particles are orientationally dependent. The nano- and microscale particles have attracted significant research interest due to their diverse morphology, for instance, asymmetry in composition or shape as well as the difference in polarity or polarisability within an individual particle[16]. These particles can possess a high number of surface regions ordered in a symmetrical manner, called patches[17]. Figure 1.1 shows classification of anisotropic particles: a) surface anisotropy and b) particle shape anisotropy[2]. The class of surface anisotropic particles feature re-configurable and directional interactions between the particles due to the presence of patches.

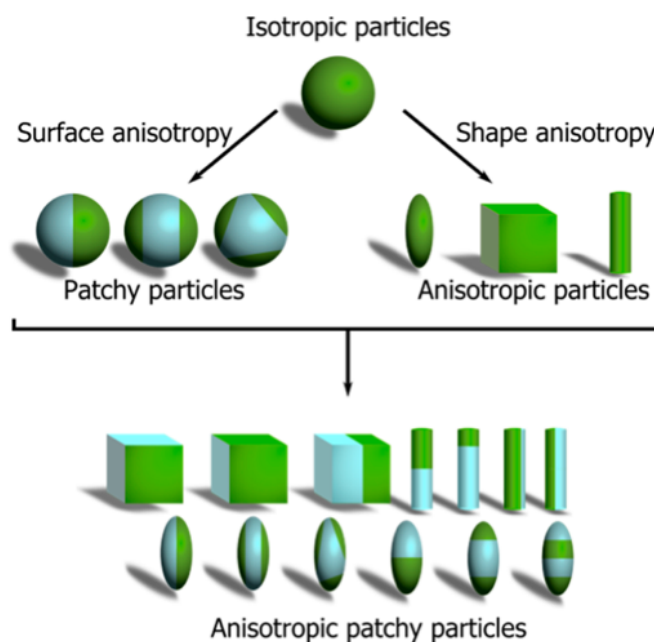


Figure 1.1: *The classification of anisotropic particles divided into two groups: a) surface anisotropy and b) particle shape anisotropy. Anisotropic molecules can be further subdivided by combining surface and shape anisotropy - reproduced from reference[2].*

Among all the broad diversity of self-assembly, the focus of this research studies explicitly the self-assembly of bipatchy particles. This thesis focuses on particular patchy particles possessing patches with opposite charge signs localised at the poles. These particles can be produced by chemical functionalisation or printing in terms of patches.

Bipatchy and monopatchy particles with attractive regions (force generated on

one bipatchy particle that attracts another bipatchy particle) lead to patch-to-patch interactions with other patchy particles and demonstrate self-organisation into higher-order systems, including chains, rings and more complex twisted structures or even diamond lattice arrangements[1, 4, 18, 19]. Such a feature of self-assembly can be employed in building higher-order specific target structures[20–22]. The ability to tune the patch’s size, shape and distribution, and thus controlling the directionality of interactions between the particles, can allow studying the aggregation behaviour in biological systems and practical applications such as photonic materials and drug delivery[23–26]. The fabrication of a patch on a bipatchy particle surface remains a challenge due to the precision and accuracy of patch location during a large production. Recent developments in experimental routes include a stamping technique using the Glancing Angle Vapor Deposition method and sandwich microcontact printing (also called microcontact printing). The former method required two steps to produce patches at the particle poles when using a polydimethylsiloxane (PDMS) stamp[27]. The technique inverts the particle with the patch facing down produced by the first vapour deposition. The patch parameters can be adjusted by positioning the template and the beam angle. The sandwich microcontact printing method, on the other hand, requires one step to generate patches on the particle’s surface by also using PDMS stamps. The stamp is ”inked” (coated) with molecules, and then it transfers the ink onto a colloidal particle[28].

In 2020 Mehr et al.[1] successfully synthesised inverse bipatchy microcolloids via sandwich microcontact printing method. Two oppositely charged polymeric patches poly(methyl vinyl ether-alt-maleic acid) (PMVEMA) and polyethyleneimine (PEI), were generated on polymer melamine formaldehyde (MF) particle’s surface. The self-aggregation behaviour of monopatchy and bipatchy microparticles in solutions has been studied to explore the reversible electrostatic interactions. The patches have been electrostatically attached to

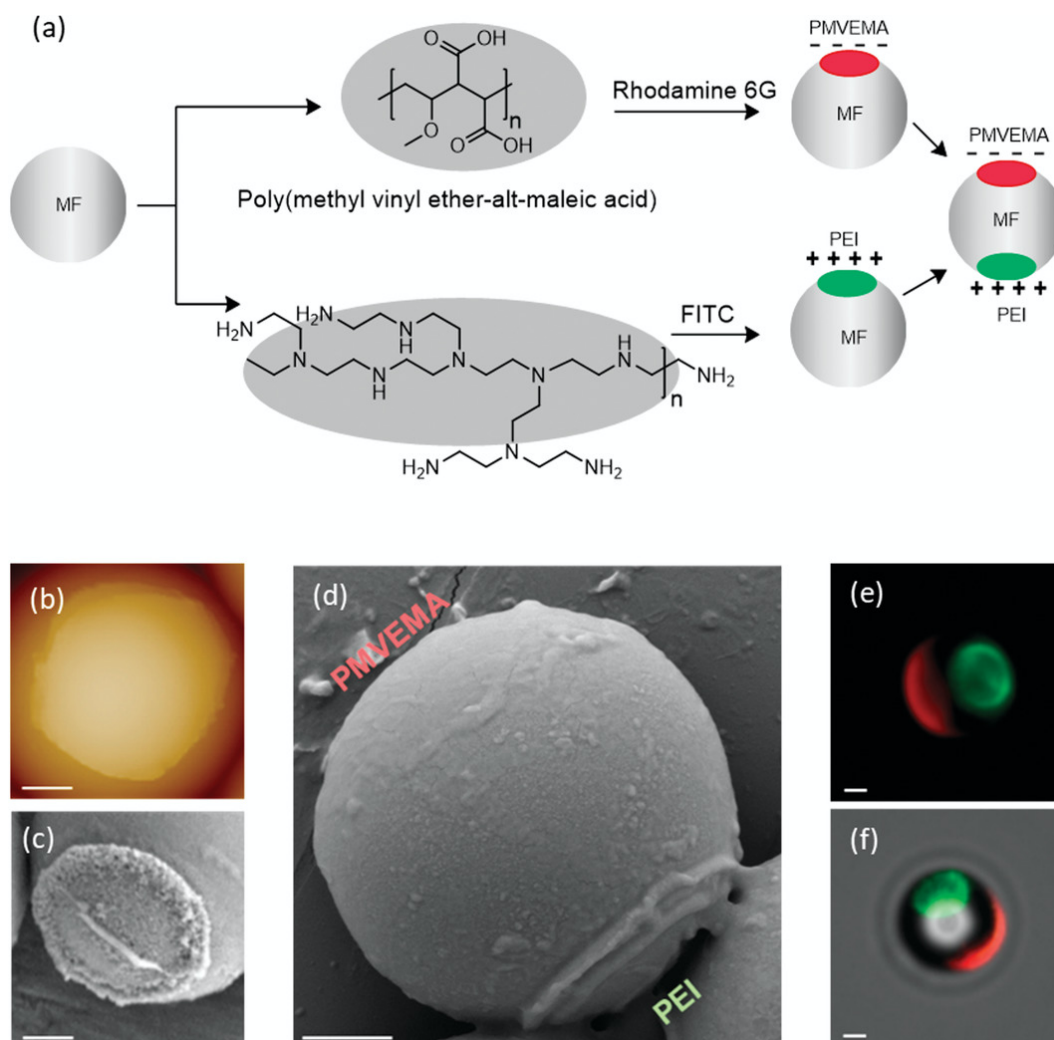


Figure 1.2: a) Reaction schemes of the production of the oppositely charged patches on the surface of an MF particle made of pre-labeled PMVEMA and PEI with Rhodamine 6G and FITC, respectively. b) SFM height image of a PMVEMA patch. c) SEM image of a PEI patch. d) SEM image of a bipatchy MF particle. e, f) fluorescence and the overlaid microscope images of bipatchy MF particles with patches made of PMVEMA (red) and PEI (green). Scale bars: $1 \mu\text{m}$ - reproduced from reference[1]

the primary particle's surface. Several microscopic images present the attachment of patches onto the MF particle; Figure 1.2 shows images of PEI and PMVEMA patches (labelled with Rhodamine 6G and fluorescein isothiocyanate (FITC) tags) and the creation of oppositely charged inverse bipatchy particles generated by fluorescence microscopy. The self-aggregation of bipatchy particles into linear, bent and branched chains of different lengths was reported. The self-assembly of patchy colloidal particles is driven by the attractive electrostatic force generated between patches and the polarisation of charge density. Figure 1.3 summarises the experimental observations of what patches have been found facing one another and the percentages of relative orientations. The self-assembly also occurs between like-charged patches with percentages of 11 and 9 for PEI-PEI and PMVEMA-PMVEMA connection, respectively. The higher yield of PEI-PEI connections can be explained due to the smaller magnitude and density of charge on the patches in comparison to the negatively charged PMVEMA patches. Oriented patch-central MF particle and MF-MF connections were also reported. The presence of patches carrying the positive and negative charge, polarised MF neutral particles as well as the medium influenced the charge distribution of the MF particle.

A variety of models have been proposed throughout the years to study problems concerning electrostatic interactions and are widely applied to investigate yet not fully understood fundamental reactions in natural sciences and industrial sectors[29–33]. The formation of PEI-PMVEMA pair interactions and patch-MF particle connections were also analysed computationally by E.Besley and her group[1]. In this work, a bipatchy particle is represented by three spheres: smaller particles are attached to the mother MF particle poles. The smaller spheres that model the patches have their charge and dielectric constant, k . The effect of monopatchy and bipatchy particles relative orientations were studied as a function of their surface-to-surface separation. The simulations were carried out by using the numerical solution proposed by Lindgren et al.[3]

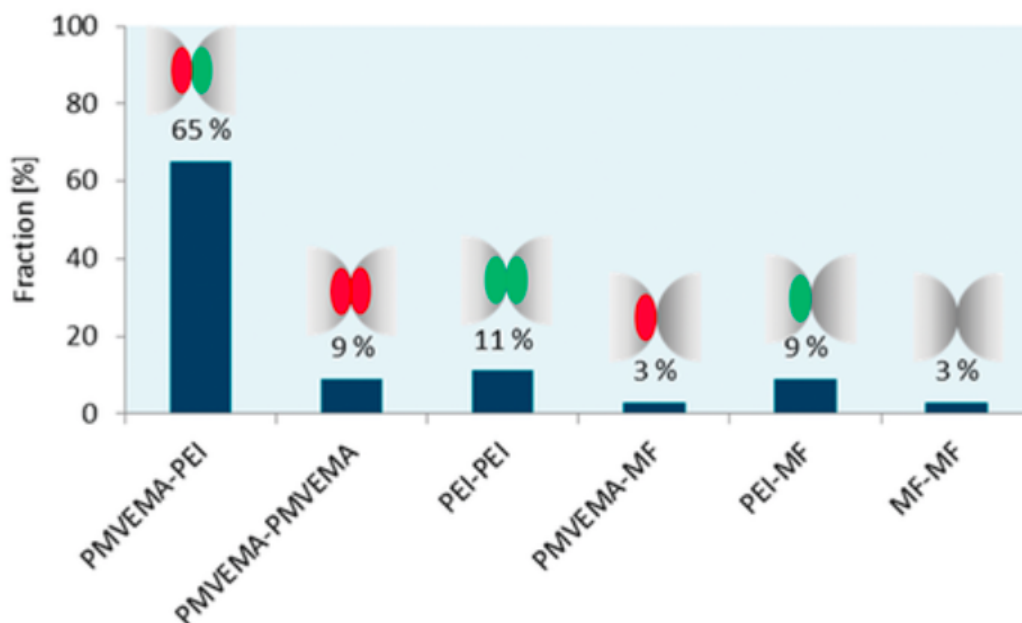


Figure 1.3: *Particles connections formed via random interactions between patchy and non-patchy surfaces of MF particles, together with % of experimentally observed connections in the aggregates formed by MF particles. The fraction of PEI patch interactions is larger than the fraction of PMVEMA interactions due to the higher yield of PEI patches - reproduced from reference[1]*

described in section 2.3.

However, the three-body approach as a representation of a bipatchy particle has its limitations. The smaller particles that represent patches, in fact, limit the distance between the central MF particles, which experimental outcome summary shows that the MF particles appear to be at a closer distance than the PEI or PMVEMA particle's size in the three-body model. Moreover, the three-body approach does not reflect realistic distances at all orientations of the bipatchy particles when comparing to the experimental data. Furthermore, the patches modelled by the smaller particles do not accurately represent the charge distribution of patches; Thus, the model limits the polarisation of charge on bipatchy particles. Finally, a patch modelled by a sphere is unable to reproduce the exact parameters of a patch given in the experimental results.

This research aims to approximate the patches more realistically and improve the computational modelling of the systems - modelling patches (their shape

and size) with a more approximate match to the experimental data. Thereby, the project attempts to elucidate the mechanisms of the self-assembly of patchy particles. The work in this thesis presents a computational analysis of electrostatic interactions between bipatchy particles reported by Mehr et al.[1] using higher-order Gaussian distribution of charge as a representation of patches on MF particle. Chapter 2 introduces the theory applied in modelling in Mehr et al. and this research. The section begins with introduction of dielectric materials and initial development of the electrostatic solution for two-body system by Bichoutskaia et al.[34] in 2010. Afterwards, subsequent development of the theory by Lindgren et al.[3] in 2018 is introduced; the model enables to calculate many-body systems. Following this, chapter 3 presents the theory behind the modelling of a patch on a particle's surface and numerical validations supporting the implementation of the model. Chapter 4 shows the predictions for the computational analysis of the experimental work published by Mehr et al.. As an additional extension of this project, atomic-scale interactions were modelled of charged diatomic molecules using dielectric spheres, and the accuracy of the many-body classical model used in this research was evaluated - an introduction and results are presented in appendix B.

Chapter 2

Theoretical background to modelling electrostatic interactions

In this chapter, the theoretical models of electrostatic interactions are presented, which treat the particles as dielectrics that are known to have classical polarisation properties.

2.1 Polarisation in dielectrics

Each material has its unique physical properties. In materials with mobile charge carriers, electric current conduction occurs under the influence of an electric field, and those are referred to as conductors. Materials that are absent of free carrier are insulators. Dielectrics, a class of insulators, poorly conduct the electric charge due to either low mobility of the charge carriers or their low concentration, or both. When a dielectric material is exposed to an electric field, dipoles are generated, or the existing dipoles align themselves within an electric field. In addition to this type of polarisation, called orientation polarisation, three other divisions of polarisation mechanisms exist: electronic (charge distribution in relation to the nucleus under the influence of the electric field),

ionic (displacement of positive and negative ions relative to each other under the influence of an electric field) and interfacial (inhomogeneous distribution of space charge due to the restriction of the charge movement).

One more crucial physical quantity that determines the ability of a dielectric material to polarise is the electric susceptibility of the medium. The electric susceptibility χ_e is a dimensionless coefficient of proportionality between the polarization density \mathbf{P} and the electric field \mathbf{E} . The electric susceptibility and vacuum permittivity ε_0 are related in a form:

$$\mathbf{P} = \varepsilon_0 \chi_e \mathbf{E}. \quad (2.1)$$

The electrical displacement \mathbf{D} can be expressed by the electrical susceptibility and strength of the electric field in the form:

$$\mathbf{D} = \varepsilon_0 \mathbf{E} + \mathbf{P} = \varepsilon_0 (1 + \chi_e) \mathbf{E} = \varepsilon_r \varepsilon_0 \mathbf{E} = \varepsilon \mathbf{E}. \quad (2.2)$$

where $\varepsilon = \varepsilon_r \varepsilon_0$, and $\varepsilon_r = (1 + \chi_e)$.

The Laplace equation is critical when solving electrical potential problems, and being expressed as:

$$\nabla^2 \Phi = 0, \quad (2.3)$$

where Φ is the electric potential. The relationship between electric potential and electric field can be defined as $\mathbf{E} = -\nabla \Phi$, following Gauss's law, $\nabla \cdot \mathbf{D} = \rho_f$.

The Laplace equation can be only solved with the set of well defined boundary conditions on the electric field and dielectric displacement field.

Numerous solutions for calculating the electrostatic forces between dielectric particles have been presented over the last decades. Although the proposed

models are diverse in the approach of calculating electrostatic forces, these solutions often converge poorly at the short-range separation between particles and are only suitable in certain circumstances. Many models are based on the image charge theory or multipole expansion method[35–38]. An adequate mathematical model is essential to determine the physical quantities characterizing interactions between charged dielectric particles and dielectric interfaces. The following sections, introduce the theory behind the model that has been used in this work and in work presented by Mehr et al.[1].

2.2 Two-body polarisable electrostatic solution

In 2010 Bichoutskaia et al.[34] proposed a general solution for calculating electrostatic interactions between two interacting dielectric spheres. The method uses multipole expansion of the potential in Legendre polynomials for a system with two dielectric particles with spherical coordinates ($i = 1, 2$). The interacting particles are of arbitrary radius a_i and charge q_i placed in a dielectric medium k_0 with their own dielectric constant k_i at particle surface-to-surface separation s . The centre-to-centre separation h between two spheres is defined as $h = s + a_1 + a_2$. The free charge is uniformly distributed on a particle's surface $\sigma_f = q/(4\pi a^2)$ with no presence of volume charge distribution. The model is also formulated on the electric potential to vanish at infinity and includes a number of boundary conditions. The first condition states that the potential generated on the sphere's surface is continuous, and thus the tangential component of the electric field is also continuous,

$$\hat{\mathbf{n}} \times \left(\mathbf{E}_{r_i=a_i^+} - \mathbf{E}_{r_i=a_i^-} \right) = 0. \quad (2.4)$$

The second boundary condition says that due to each sphere carrying a permanent charge on its surface σ , the normal component of the electric field is

discontinuous,

$$\hat{\mathbf{n}} \cdot \left(\mathbf{E}_{r_i=a_i^+} - \mathbf{E}_{r_i=a_i^-} \right) = \frac{\sigma}{\varepsilon_0}. \quad (2.5)$$

The third boundary condition postulates that due to the presence of free charge on a sphere's surface σ_f , the normal component of the electric displacement field is discontinuous,

$$\hat{\mathbf{n}} \cdot \left(\mathbf{D}_{r_i=a_i^+} - \mathbf{D}_{r_i=a_i^-} \right) = \sigma_f. \quad (2.6)$$

where $\hat{\mathbf{n}}$ is defined as unit vector and located at 90° to a point on a sphere. The electric displacement field \mathbf{D} is characterised by equation (2.2). The a_i^+ and a_i^- are the radial positions for particles (can be positioned inside and outside).

Following this, the electrostatic force is calculated based upon Coulomb's law, and its extension relevant for this two-body problem. For a system with two point charges ($i = 1, 2$) individually positioned \mathbf{r}_i and possessing separate charge q_i . Considered system is in a vector form, and placed in vacuum. Thus, an electrostatic force \mathbf{F}_1 acting on q_1 is equal to:

$$\mathbf{F}_1 = \frac{q_1 q_2}{4\pi\varepsilon_0} \frac{\mathbf{r}_1 - \mathbf{r}_2}{|\mathbf{r}_1 - \mathbf{r}_2|^3} = \frac{q_1 q_2}{4\pi\varepsilon_0} \frac{\hat{\mathbf{r}}_{12}}{|\mathbf{r}_{12}|^2}, \quad (2.7)$$

where $\mathbf{r}_{12} = \mathbf{r}_1 - \mathbf{r}_2$ and $\hat{\mathbf{r}}_{12} = \frac{\mathbf{r}_{12}}{|\mathbf{r}_{12}|}$ - a unit vector from q_2 to q_1 . The electrostatic force that acts on q_2 is equivalent to $\mathbf{F}_2 = -\mathbf{F}_1$ (as stated by Newton's third law).

A particle with a charge q_i in a presence of the electric field \mathbf{E} will experience the electrostatic force \mathbf{F} given as:

$$\mathbf{F} = q\mathbf{E}. \quad (2.8)$$

Coulomb's law states that the generation of the electric field \mathbf{E}_i at position \mathbf{r}_0

caused by the presence of a point charge q_i located at \mathbf{r}_i can be described as:

$$\mathbf{E}_i(\mathbf{r}_0) = K \frac{q_i}{|\mathbf{r}_0 - \mathbf{r}_i|^2} \hat{\mathbf{r}}_{0i}, \quad (2.9)$$

where K is Coulomb's constant $1/(4\pi\epsilon_0)$ (ϵ_0 is the vacuum permittivity). In a case of two spherical particles with uniformly distributed charge on the particles' surface and amount of the electrostatic force \mathbf{F}_{12} between the two objects is given by:

$$\mathbf{F}_{12} = K \int dq_1(\mathbf{r}_1) \int dq_2(\mathbf{r}_2) \frac{\hat{\mathbf{r}}_{12}}{|\mathbf{r}_1 - \mathbf{r}_2|^2}, \quad (2.10)$$

where K is Coulomb's constant, $dq_1(\mathbf{r}_1)$ and $dq_2(\mathbf{r}_2)$ are the charges placed on each particle, and \mathbf{r}_1 and \mathbf{r}_2 are position vectors at each particle. The charge on particle 1 is described by $\int dq_1(\mathbf{r}_1)$ and the electric field produced by the charge on the second particle defines the remaining components of the equation 2.10.

Using equation 2.10 and a Legendre polynomial expansion of the electric potential Φ (generated by the charges) the electrostatic force between two particles ($i = 1, 2$) can be calculated. The surface charge density on a particle's surface is expressed by vector h . The following equation enables one to calculate the amount of electrostatic force generated between two spheres subsequently after the integration of charge over the surface area of the particles, as shown:

$$\mathbf{F}_{12} = -\frac{1}{K} \sum_{l=0}^{\infty} A_{1,l} A_{1,l+1} \frac{(k_1 + 1)(l + 1) + 1}{(k_1 - 1)a_1^{2l+3}}. \quad (2.11)$$

Obeying Coulomb's law, a positive value of \mathbf{F}_{12} indicates repulsion between two particles; thus the negative value indicates attraction between the bodies. The electrostatic force generated between two particles at a separation h depends on the multipole moment coefficients $A_{1,l}$ and $A_{1,l+1}$. Taking into account the remaining variables of the interacting spheres that accounts for the mutual influence of polarisation of the particles, the expression that describes the

multipole moment coefficients $A_{1,l}$ and $A_{1,l+1}$ is expanded to:

$$\begin{aligned} \mathbf{F}_{12} = & K \frac{q_1 q_2}{h^2} - q_1 \sum_{m=1}^{\infty} \sum_{l=0}^{\infty} A_{1,l} \frac{(k_2 - 1)m(m+1)}{(k_2 + 1)m + 1} \\ & \times \frac{(l+m)!}{l!m!} \frac{a_2^{2m+1}}{h^{2m+l+3}} - \frac{1}{K} \sum_{l=1}^{\infty} A_{1,l} A_{1,l+1} \frac{(k_1 + 1)(l+1) + 1}{(k_1 - 1)a_1^{2l+3}}. \end{aligned} \quad (2.12)$$

Equation (2.12) can be broken down into three terms. The first considers the interaction between a pair of monopoles. The remaining terms describe the mutual polarisation of charge on the particles' surface. An attraction will arise when the system is in a vacuum, and its strength depends on the dielectric constant k_i of the particles. Furthermore, like-charged particles can also experience Coulombic attraction when set in a specific environment (q_i , a_i , and k_i variables influence the polarisation of charge density). Combining those variables can cause the total net of the interaction to be attractive at a touching point for like-charged objects due to a mutual polarisation of their charge density.

Since 2010, the model has been expanded and accounts for many-body systems, and thus increased its applications, including the aggregation of charged dust and ice particles in the atmosphere, aggregation of pharmaceutical aerosols (static as well as dynamic simulations), self-organisation of macroanions (polyoxometalates).

2.3 Many-body polarisable electrostatic solution

In 2018 Lindgren et al.[3] introduced a model to calculate electrostatic interactions for many-body polarisable systems. The theory is based upon an integral equation approach that enables one to calculate systems consisting of M non-overlapping particles placed in the three-dimensional space \mathbb{R}^3 . Those

spherical particles can have arbitrary size (radii defined as $\{a_i\}_{i=1}^M$ and centered at $\{\mathbf{x}_i\}_{i=1}^M$), a free charge q_i as well as dielectric constant $\{k_i\}_{i=1}^M$ (where $k_i \geq 1$) surrounded by homogeneous medium of dielectric constant $k_0 \geq 1$ (where $k_0 \geq 1$), as shown in figure 2.1. This method includes a modified fast multipole method.

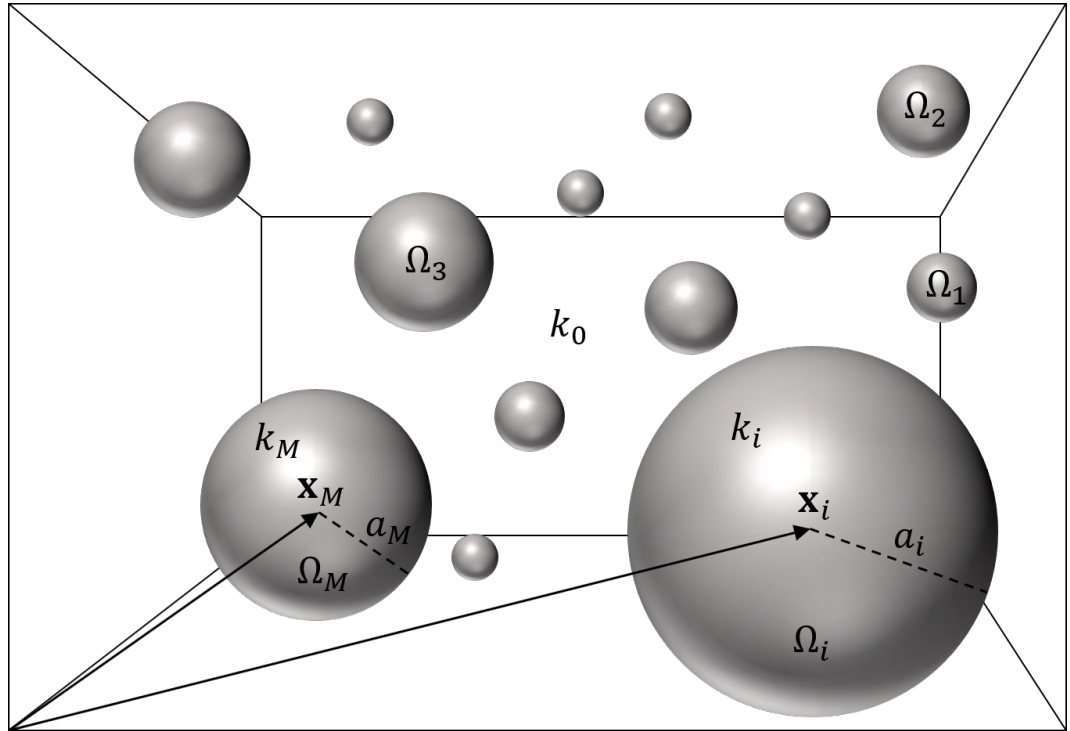


Figure 2.1: Geometric representation of the many-body system Ω_M with radius \mathbf{a}_i and centred at x_i , dielectric constant k_i , in a homogeneous medium of dielectric constant k_0 [3].

A system of spherical particles $\{\Omega_i\}_{i=1}^M$, where the particle's surface is represented by $\{\Gamma_i\}_{i=1}^M$ and Γ represents the boundary - the surface of the sphere (the charge is only applied within the particle's surface), and for that:

$$\Gamma_0 = \Gamma_1 \cup \dots \cup \Gamma_M.$$

A free charge density is uniformly distributed over the particle's surface Γ with

no volume charge present. The surface charge density is represented as:

$$\sigma_{f,i} = \frac{q_i}{4\pi r_i^2}, \quad (2.13)$$

where the free charge σ_f obeys a boundary condition:

$$\sigma_f(x) = \begin{cases} \sigma_{f,i}, & \text{if } x \in \Gamma_i. \\ 0, & \text{otherwise.} \end{cases} \quad (2.14)$$

In addition, a surface charge density σ_f satisfies three interface boundary conditions defined in equations (2.4)-(2.6).

Following, the free charge σ_f that generates the electrostatic potential $\Phi \in L^2_{loc}(\mathbb{R}^3)$ with $\Phi|_{\Omega_i} \in H^1(\Omega_i)$ which satisfies given boundary conditions:

$$\Delta\Phi = 0 \quad \text{in each } \Omega_i, \quad (2.15)$$

$$[[\Phi]] = 0 \quad \text{on } \Gamma_0, \quad (2.16)$$

$$[[k\nabla\Phi]] = 4\pi K\sigma_f \quad \text{on } \Gamma_0, \quad (2.17)$$

where K is Coulomb's constant. The $[[k\nabla\Phi_{\text{tot}}]]$ are jump discontinuities, and they are defined as:

$$[[\Phi]]|_{\Gamma_i}(x) = \Phi|_{\Omega_0}(x)n_0(x) + \Phi|_{\Omega_i}(x)n_i(x), \quad (2.18)$$

$$[[k\nabla\Phi]]|_{\Gamma_i}(x) = (k\nabla\Phi)|_{\Omega_0}(x) \cdot n_0(x) + (k\nabla\Phi)|_{\Omega_i}(x) \cdot n_i(x), \quad (2.19)$$

where $x \in \Gamma_i$, and $n_0(x)$ defines the outward pointing normal to Ω_i for $x \in \Gamma_i$.

The total energy U of a considered many-body system is given by:

$$U(\Phi, \sigma_f) = \frac{1}{2} \int_{\Gamma_0} \sigma_f(s)\Phi(s)ds, \quad (2.20)$$

where s is a point of integration on the particle's surface. Both, Φ and σ_f account for the total energy U , where the former is generated due to the

neighbouring particles.

The solution has the capability of using the modified Fast Multipole Method (FMM). The method accelerates the calculations by applying a linear scaling algorithm in relation to the system complexity. This process allows to efficiently converge at a touching point of the spheres without significant computational cost increase. Furthermore, FMM supplies quantitative information about the physical nature of the system. The algorithmic description can be found in Lindgren et al.[3].

Its fast convergence even at a touching point of charged particles distinguishes this method and the low cost of calculations compared to other proposed solutions. Those often use the previously explained method of image charges or are based on a multipole expansion method. The multipole expansion method has the advantage of showing how the charge density is redistributed due to the presence of other charged particles. Nevertheless, those techniques require a large number of steps to complete the calculations due to the requirement to use numerous images or terms.

Chapter 3

Analytical representation of the localised surface charge; modelling a patch

This research's principal purpose is to improve the modelling of patchy particles to enable computational predictions of the patchy particle systems with increased accuracy. In 2020 Mehr et al.[1] explored computationally the interactions between patchy particles. In Mehr et al., a patch was modelled by a separate particle possessing its charge and dielectric constant, as described earlier in section 1. In this chapter, the theory behind the modelling of a patch is explained. Additionally, other models of presenting a patch on a particle's surface are discussed. Subsequently, numerical validations are presented to support the implementation of this model. As described in the introduction in current way of modelling patches is limited and there are three fundamentally different ways of reducing the limitation. It is a point charge, it is the normal Gaussian distribution of charge and it is the higher-order Gaussian distribution. A patch's size can vary from covering a substantial amount of particle surface up to a point to being concentrated at a localised point. Point charge represents one of the extremes of distributing a charge on a surface. The charge in this configuration is condensed and can even represent a single charge[7].

On the other hand, Gaussian distribution of charge and higher-order Gaussian distribution both have the ability to manipulate the size of a patch - its width. Moreover, when applying higher-order Gaussian distribution, the shape of the patch can be adjusted - its "flatness". Nonetheless, each representation has limits and unique properties, and appropriate times to be applied.

3.1 Higher-order Gaussian distribution

A sphere of radius a has the lowest energy form of a free-charge distribution q when the charge is uniformly spread over its whole surface. This uniform charge density σ_s for a spherical object is given by:

$$\sigma_s = \frac{q}{4\pi a^2}. \quad (3.1)$$

A non-uniform surface distribution of charge is often a more suitable approach when modelling systems for experimental work. Localisation of charge can be expanded to point charge solution as well as a multivariate form of a distribution. The former has particular use in studying the Coulomb fission of charged clusters and patchy colloids[28, 39]. On the other hand, the latter can be applied in modelling point charges when the standard deviation value is sufficiently small and patches on colloidal spheres (equation 3.7).

The probability density function of a Gaussian distribution with an expected value of μ and a standard deviation v is specified as:

$$f(x) = \frac{1}{v_x \sqrt{2\pi}} \exp\left(-\frac{(x - \mu_x)^2}{2v_x^2}\right). \quad (3.2)$$

If the Gaussian distribution is defined in two-dimensional domain, then the probability density function will include the vector $\boldsymbol{\mu}$ of the expected values

$\boldsymbol{\mu} = (\mu_x, \mu_y)$, and for x and y coordinates (v_x, v_y) . The two-dimensional distribution with the density function $f(x, y)$ has the form of:

$$f(x, y) = \frac{1}{v_x \sqrt{2\pi}} \exp\left(-\frac{(x - \mu_x)^2}{2v_x^2}\right) \frac{1}{v_y \sqrt{2\pi}} \exp\left(-\frac{(y - \mu_y)^2}{2v_y^2}\right). \quad (3.3)$$

In addition, in the event where the standard deviation for x and y positions are equal, the function can be shown in the form:

$$f(d) = \frac{1}{2\pi v^2} \exp\left(-\frac{d^2}{v^2}\right), \quad (3.4)$$

where the variable v represents the standard deviation for the Gaussian function, and the d variable is the distance from the two expected values $(\mu_x; \mu_y)$.

If Gaussian function is implemented to represent Gaussian surface charge density σ_g on a spherical object, the function requires to account the total charge q_g that will be distributed on its surface given by:

$$\sigma_g(d) = \frac{q_g}{2\pi v^2} \exp\left(-\frac{d^2}{v^2}\right) \quad (3.5)$$

within the area of the object's surface. Numerous Gaussian distributions are required to be used to model the density charge on a sphere accurately. Thus, for a defined location $\sigma_g(d)$ on a sphere with Gaussian functions n_g placed on its surface representing the charge distribution, the equation will take the form:

$$\sigma_g(d) = \sum_{k=1}^{n_g} \frac{q_{g,k}}{2\pi v_k^2} \exp\left(-\frac{d_k^2}{v_k^2}\right) \quad (3.6)$$

where $\boldsymbol{\mu}_k = (\mu_{x,k}, \mu_{y,k})$ within the area of the object's surface.

In equation (3.5), the variable v that represents the standard deviation also controls the width - the magnitude and the density of the charge on a particle. The larger the v , the wider the charge density distribution will become within the particle's diameter.

Furthermore, the shape of the density charge distribution curve can be altered by increasing the P value in equation (3.7). The curve will become more flat-topped when $P > 1$. The two-dimensional higher-order Gaussian distribution is represented by:

$$\sigma_g(d) = \frac{q}{2\pi v^2} \exp\left(-\left(\frac{d^2}{v^2}\right)^P\right). \quad (3.7)$$

Despite the ability to modify the density charge distribution curve, a loss of charge will occur due to the curvature of the sphere - its three-dimensional shape.

One necessary condition has to be met when distributing charge on a bipatchy particle. The arrangement of patches shall not lead the density charges to interact one with another. A test was conducted to examine at what point of a sphere two patches will start interacting with each other. Figure 3.1 shows the surface charge density at a singular point placed between two patches localised on a single particle pole a . The patch width of both patches v increases in size from 0.1 to 2. The surface charge density σ is distributed over the patch and is defined by dimensions by the size v/a . As the surface charge distribution σ on each patch enlarges and once the patches touch the singular point, the charge density starts to overlap. Thus, the largest two standard Gaussian patches of charge with circular symmetry that can be modelled (in the most energetically stable position), will have the ratio of 0.3 v/a - figure 3.1 yellow plot. The

rapid increase of the charge density arises from two patches increasing in size to a point when they start to overlap. Hence, any value of v/a higher than 0.3 for normal Gaussian will cause the surface density charges σ to overlap - as shown in figure 3.1 - or cancel out when considering unlike charges. Similarly, for higher-order Gaussian distribution $P = 2$ and $P = 5$ in equation (3.7) the limitations remain 0.55 and 0.8 v/a , respectively. The sudden increase in limitation between normal Gaussian and higher-order Gaussian distribution is due to the charge being more evenly residing on the surface when applying higher-order Gaussian distribution as clearly shown in figure 3.2. In contrast, when implementing normal Gaussian, the charge is more concentrated in the centre of the patch and more diffuse at the edges leading to loss of charge (figure 3.2a).

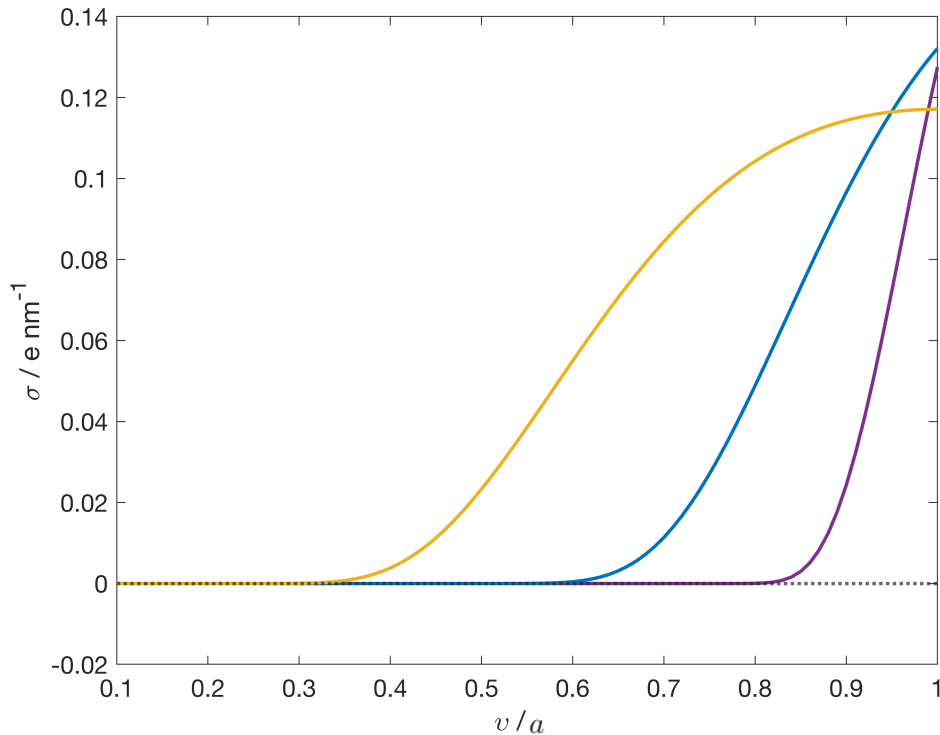


Figure 3.1: σ as function of the ratio v/a , where $q_1 = q_2 = +1e$. For $k_m = k_p = 1$ and $a = 1$ nm. Patches with normal Gaussian distribution ($P = 1$, yellow), and higher-order Gaussian distribution ($P = 2$, blue) and ($P = 5$, purple).

Oppositely, the limitation for a patch of charge to not interfere with the other

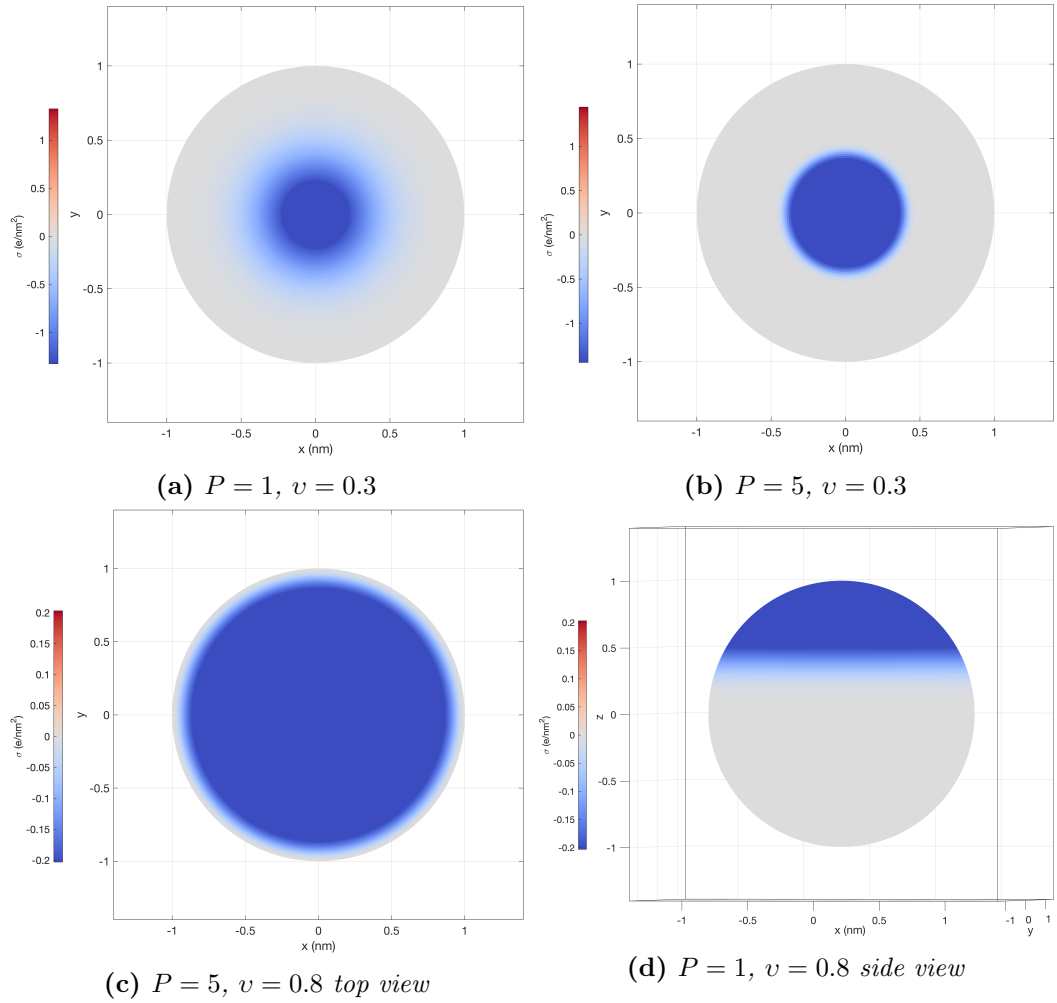


Figure 3.2: Visual representations of the surface charge density on a non-polarisable sphere $a = 1$ nm where $q = -1e$.

patch does not need to be followed when modelling mono-patchy particles. Nonetheless, the charge distribution cannot be greater than the particle's diameter to ensure that the density charge entirely remains on the particle's surface. Figure 3.3 shows interaction between two particles set at a sufficiently large separation distance $s = 1000$ nm to ensure that the interaction energy at short separation does not dominate. Particle a_1 has a Gaussian patch placed on facing the second particle. The charge on a_2 is uniformly distributed. The size of the patch on a_1 increases from 0.1 to 2. Accordingly, for a normal Gaussian distribution, the amount of charge will remain accurate for v/a_1 smaller than 0.5, as shown in Figure 3.3. Consequently, when $v/a_1 > 0.5$, then loss of charge will occur. Subsequently, when using equation (3.7) for Higher-order Gaussian distribution and the P variable is set to be equal to 2 and 5, the limitation

for v/a_1 will equal 0.9 and 1.2, respectively. Following the analogy of charge distribution between normal Gaussian and higher-order Gaussian distribution in case of bipatchy particle, the loss of charge decreases for the "flatter" patch ($P > 1$) as the charge is less diffuse.

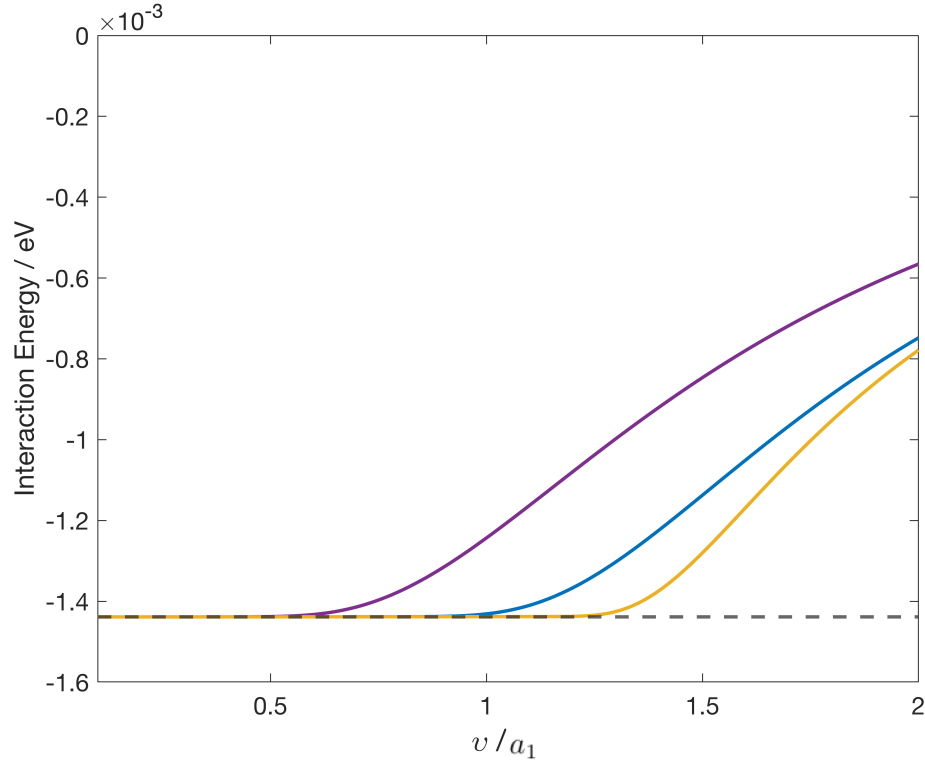


Figure 3.3: Interaction energy as a function of the ratio v/a_1 . $P = 1$ (yellow solid line), $P = 2$ (blue solid line), $P = 5$ (purple solid line), where $q_1 = +1e$ and $q_2 = -1e$. For $a_1 = a_2 = 1$ nm at $s = 1000$ nm. The dashed line represents the interaction between two point-charges $q_1 = +1e$ and $q_2 = -1e$ at $s = 1000$ nm.

As observed in figure 3.1 and 3.3, with the increase of P-value ($P > 1$), the change in the shape of the Gaussian function allows one to obtain the charge density to be less non-uniformly distributed within the patch's area. Thus, a patch can be enlarged without loss of charge. Figure 3.4 visualises how the shape of a Gaussian function changes when increasing the P value as well as varying the v value. Nonetheless, Gaussian distributions are intended for flat surfaces rather than spherical.

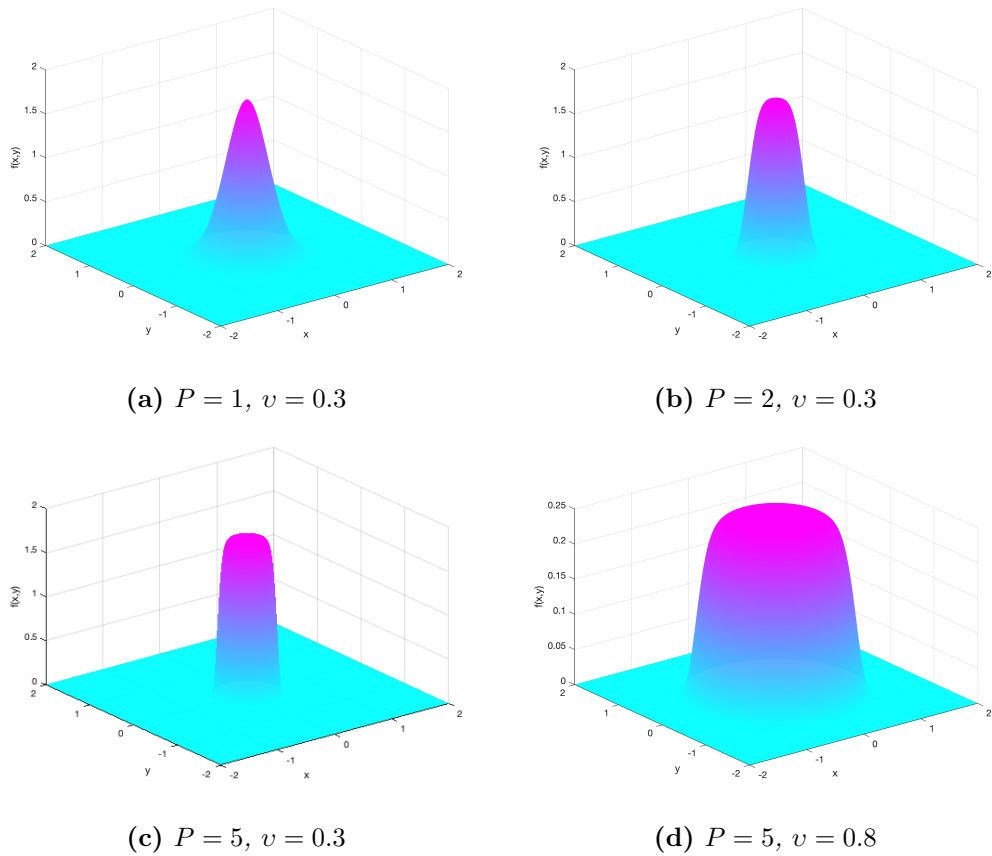


Figure 3.4: Higher-order Gaussian distribution when using equation (3.7), where $(\mu_x; \mu_y)$ is the centre.

3.1.1 Testing higher-order Gaussian distribution of charge

Coulomb's law - equation (3.8) - was applied to calculate the electrostatic potential energy of point charges at a range of separation distances and compare the results obtained using the existing model. Coulomb's law considers charge density to be a point charge on a particle's surface. When the charge density is uniform on a particle's surface, it can be approximated to be a point charge at the centre of a particle's surface, as shown in figure 3.5a. Whereas, applying the Gaussian distribution - if v is sufficiently small - it can be approximated to be a point charge at the sphere's surface (figure 3.5b). However, the point charges were set on each particle's right side for non-uniform charge distribution to keep a reasonable distance between the set point charges. The potential energy

U_e of a pair of charges located at a definite distance takes the form:

$$U_e = \frac{1}{4\pi\epsilon_0} \frac{q_1 q_2}{r}, \quad (3.8)$$

where ϵ_0 is the permittivity of free space, $q_{1,2}$ is the charge of each object and r is the distance between the charges.

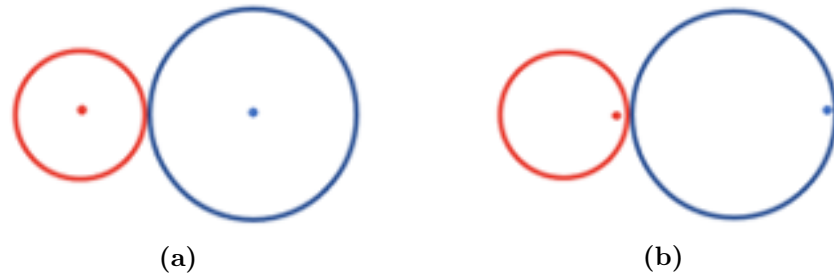


Figure 3.5: Visual representations of two point charges: (a) when the charge density is uniform, it can be approximated to be a point charge at the centre of the sphere (on the particle's surface), (b) Gaussian distribution - a patch of charge placed on the particle's surface. Red point represents a point charge with $q_1 = +1e$ and the blue dot is a point charge with $q_2 = -1e$.

Figure 3.6 represents the validation of higher-order Gaussian distribution against Coulomb's law and existing point charge and uniform distribution of charge as additional testing. The interaction energy of charged objects are calculated by using Coulomb's law and our model. The scenario to test uniform method considers two dielectric non-polarisable particles $a_1 = 1$ nm, $a_2 = 2$ nm with uniformly distributed charge over the surface of the particles, where $q_1 = +1e$, $q_2 = -1e$. The scenario for charged objects to test the uniform method is visualised in figure 3.5a. The agreement between the uniform distribution of charge using our code (figure 3.6 - orange dotted plot) and the electrostatic potential energy calculated for a pair of point charges (figure 3.6 - solid orange plot) indicates that the application of our model agrees with the expected values. Similarly, the results generated for point charges localised on a particle's surface (figure 3.6 - purple circle plot) - visualisation 3.5b also precisely meet the calculated Coulombic interactions (figure 3.6 - solid purple plot) - visualisation 3.5b. To test the higher-order Gaussian distribution of

charge the Gaussian patches were set to face the same direction to match the case for the charged objects are calculated by using Coulomb's law 3.5b. Thus, two monopatchy particles of radius $a_1 = 1$ nm, $a_2 = 2$ nm interact, where $q_1 = +1e$, $q_2 = -1e$. When implementing a higher-order Gaussian distribution of charge (figure 3.6 - purple dotted plot), the results also show a very close match to the coulombic interaction (figure 3.6 - solid purple plot). Notably - the results can be easily altered when changing the width of the patch.

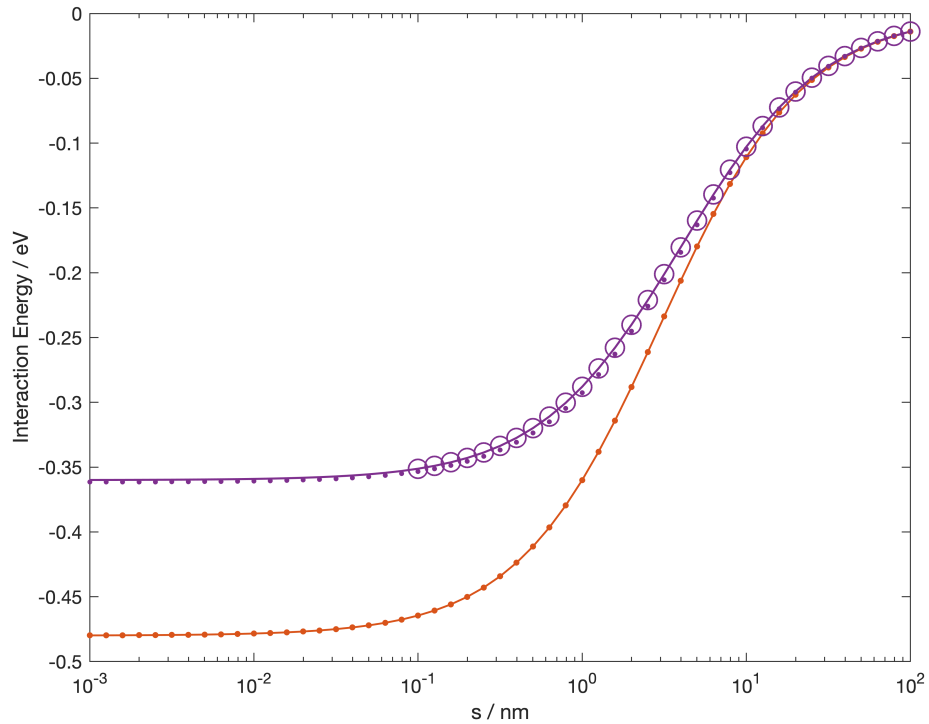


Figure 3.6: Interaction energy as a function of surface-to-surface separation s for uniform method (the potential energy equation (3.8) - orange solid, model's results - orange dots); Gaussian method (the potential energy equation (3.8) - purple solid, model's results - purple dots), the Gaussian patches on a_1 and a_2 are facing the same direction, $P = 5$ and $v/a_1 = 0.8$; results for point charge model's results - purple circles. Position of the point charges - figure 3.5. Remaining variables: $a_1 = 1$ nm, $a_2 = 2$ nm, where $q_1 = +1e$, $q_2 = -1e$ for $k_m = k_p = 1$.

As demonstrated above, the patch charge becomes more uniformly spread over the surface as increasing the P variable in higher-order Gaussian distribution. Following the presented tests, one more evaluation was carried out. Figure 3.8 shows the interaction between two bipatchy particles, each carrying two patches with an opposite sign $q_1 = +1e$ and $q_2 = -1e$ (visualisation - figure 3.7). A sig-

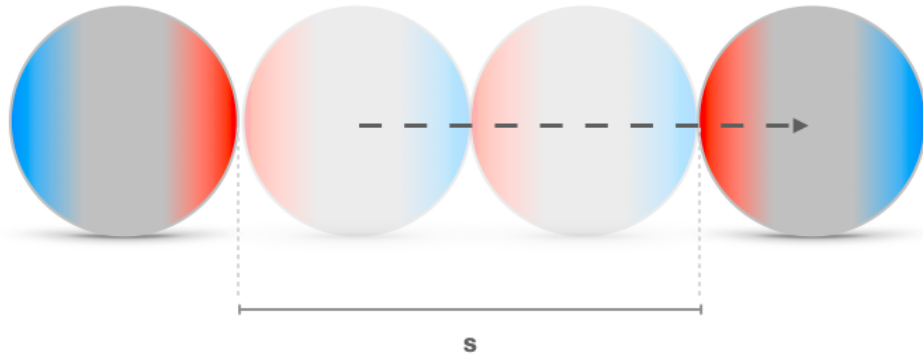


Figure 3.7: A geometric representation of two-body system. Each sphere has two oppositely charged patches with $q_1 = +1e$ (red patch) and $q_2 = -1e$ (blue patch) placed on a particle's surface. The second sphere moves away from the first sphere with surface-to-surface separation distance s .

nificant increase in interaction energy can be seen in figure 3.8 when the patches become slightly flatter on each of the bipatchy particles (P -value increases to 2). And as result the charge density becomes less dispersed. Comparing normal Gaussian distribution ($P = 1$) and higher-order Gaussian distribution ($P = 5$), the difference in the interaction energy increases by more than half its value. In addition, the energy starts to converge quicker as $P > 1$, to a point that the results almost overlap when looking at $P = 4$ (black plot) and $P = 5$ (cyan plot) - figure 3.8.

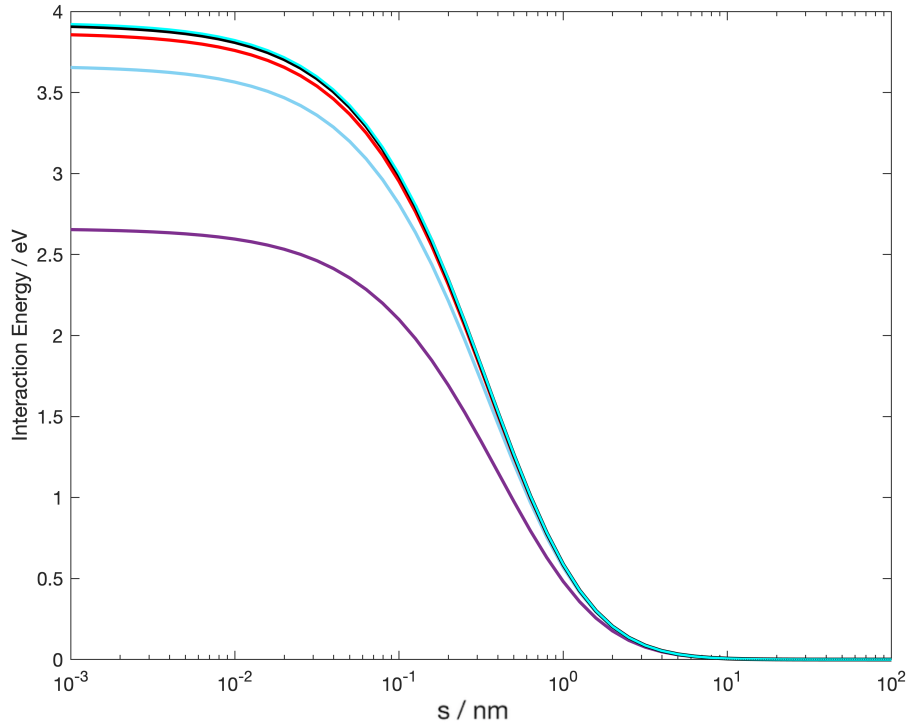


Figure 3.8: Interaction energy plots between two bipatchy particles (figure 3.7) as a function of surface-to-surface separation s for $P = 1$ (purple), $P = 2$ (blue), $P = 3$ (red), $P = 4$ (black), $P = 5$ (cyan) using equation (3.7); $k_m = k_p = 1$, $a_1 = a_2 = 1$ nm.

3.2 Numerical validations

A set of calculations was run to examine the higher-order Gaussian method of distributing charge on bipatchy particles surface. The following figures display trends and patterns with varying standard variables: the size of particles as well as the size of the patches, charge ratio, surface-to-surface separation distance and angle between two spheres. The bipatchy particles are suspended in a vacuum $k_m = 1$. The dielectric constant of the bipatchy particles k_p equals 20. The specific parameters were set to enable the charge density to sufficiently polarise on the particle's surface. The presented results of electrostatic forces and interactions in the chosen systems display a likelihood of stability for bipatchy particles at zero separation distance. Also, a series of systems are examined to test what modifications favour reducing the magnitude of repulsive

interactions between like charges.

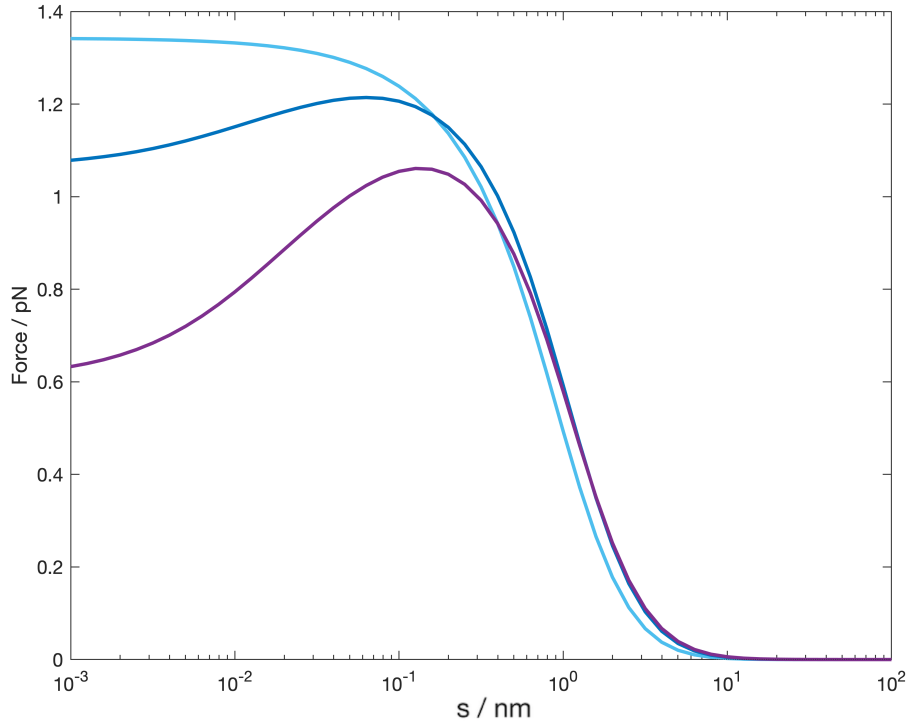


Figure 3.9: *Electrostatic force as a function of surface-to-surface separation s between two bipatchy particles (figure 3.7). Patch geometry is defined by $\nu = 0.8$ and $P = 5$ using equation (3.7). For $a_1 = 1$ nm, $k_p = 20$, $k_m = 1$ and $a_2 = 1$ nm (light blue), $a_2 = 2$ nm (dark blue), $a_2 = 3$ nm (purple).*

The electrostatic force and interaction energy were calculated between two bipatchy particles each possessing oppositely charged patches $q_1 = +1e$ and $q_2 = -1e$ (visualisation - figure 3.7) as a function of surface-to-surface separation s between two bipatchy particles. One of the bipatchy particles has a fixed size $a_1 = 1$ nm, whereas the second bipatchy particle increases in size from $a_2 = 1$ nm to $a_2 = 2$ nm and next to $a_2 = 3$ nm. The size of bipatchy particles with the fixed size of the patches while the radius of a sphere varies in size has a consequential effect on the electrostatic force - figure 3.9, for the like charges positioned adjacent to each other - figure 3.7 (visualisation). The increase in size of a_2 decreases the electrostatic repulsion, resulting in a local minimum at zero separation distance (figure 3.9 - dark blue and purple plot). Nevertheless, each system remains purely unstable - the electrostatic

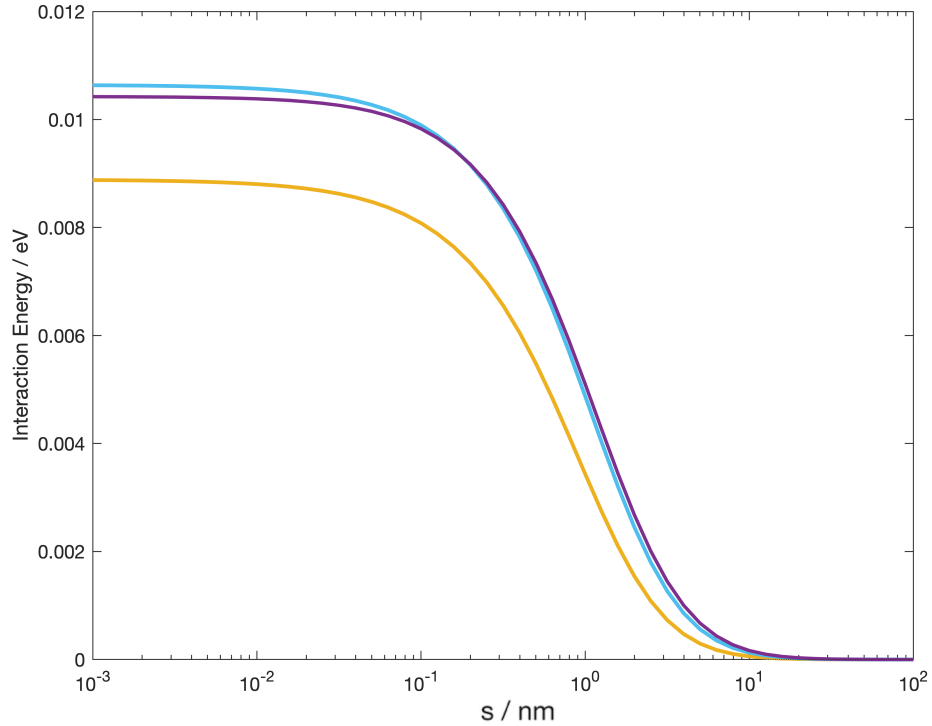


Figure 3.10: Interaction energy as a function of surface-to-surface separation s between two bipatchy particles (figure 3.7). Patch geometry is defined by $v = 0.8$ and $P = 5$ using equation (3.7). For $a_1 = 1$ nm, $k_p = 20$, $k_m = 1$ and $a_2 = 1$ nm (yellow), $a_2 = 2$ nm (blue), $a_2 = 3$ nm (purple).

interaction energy plots display a global maximum at the shortest separation distance (figure 3.10). As the system becomes asymmetric - a_2 increases in radius, the repulsive interaction increases in magnitude.

Unlike when the patch size is set to increase along with the particle's size, the system gains an attractive part of the electrostatic force at a shorter separation distance - appendix A.1. The interaction remains repulsive for a system with identical parameters of bipatchy particles due to the symmetrical charge distribution producing equal induced bound charges (appendix A.1 - light blue plot). For the systems with $a_2 = 2$ nm (dark blue plot) and $a_2 = 3$ nm (purple plot) the attractive regime appears at a short separation distance between bipatchy particles and significantly increases when the particles are positioned at a touching point. The system with symmetrical bipatchy particles remains unstable at a touching point and possesses a global maximum, that indicates that the

particles would push each other away (appendix A.2 yellow plot). When a_2 becomes twice as large than a_1 , including patch geometry, appendix A.2 (blue plot) shows a low barrier at a touching point due to the decrease of the surface density charge on a_2 . For a system with parameters of $a_1 = 1$ nm and $v = 0.8$ and the second particle a_2 increases triple in size of the radius along with the patch size, the systems gains an energetically favourable state at zero separation (purple plot). The system becomes stable at a touching configuration due to the even greater magnitude of polarisation of surface charge density on a_2 . The trend is due to the decrease of the surface density charge on the larger particle.

Similarly, the increases in the magnitude of charge and density of charge on a_2 result in a stable configuration when two bipatchy particles are at the point of contact - figure 3.11. As the patch charge increases, both - the patch charge becomes more polarisable, and the repulsive electrostatic force increases in magnitude. The latter nevertheless raises the potential energy barrier at a larger separation distance due to the increase of charge density. Thus, the purple plot has a higher barrier to separation in comparison to the green plot.

Following the studying of two-body systems at a range of separations, the analysis increases to small clusters still at varying surface-to-surface separation distances. An increase in the number of bipatchy particles in the chain immediately forms a stable system at all ranges of separation distances - figure 3.12. When the two like-charged patches are moved close to each other, the interaction energy starts repulsive, but the energy gradually becomes more and more attractive as the number of particles increases in the chain. The repulsive Coulomb term increases in magnitude at approximate 1 nm, but the systems remain at an energetically favourable position apart from the two-body system, where the Coulombic attraction entirely diminishes at a 1 nm separation distance. In addition, every next addition of a bipatchy particle lowers the interaction energy of the system with yet greater magnitude.

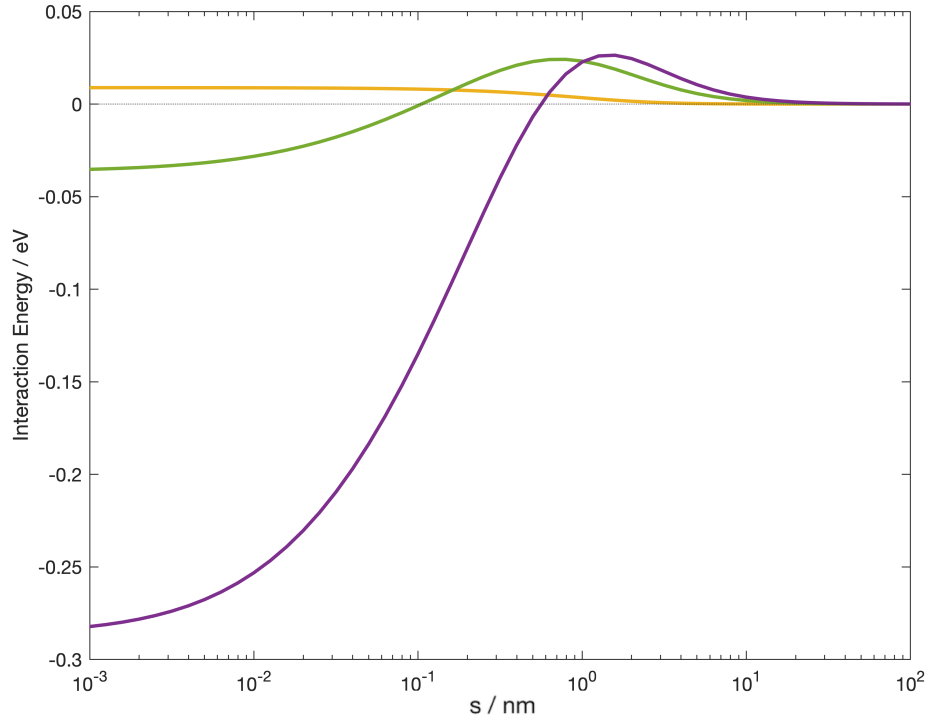


Figure 3.11: Interaction energy as a function of surface-to-surface separation s between two bipatchy particles (figure 3.7). Patch geometry is defined by $\nu = 0.8$ and $P = 5$ using equation (3.7). For $a_1 = a_2 = 1$ nm, $k_p = 20$, $k_m = 1$. The charge vary on a_2 : $q = +1e$ (yellow), $q = +2e$ (green), $q = +3e$ (purple).

The results of cluster geometry shown in figure 3.13 also present favourable interaction at all separation range. When the same sign patches of the moving particle and the particles at a fixed position are positioned in the opposite direction (figure 3.13 yellow plot), the system possesses a small energy barrier, resulting in a local minimum at the contact point. Unlike when the particle in motion has an opposite charge patch facing the cluster, the attractive part of Coulombic interaction increases significantly in magnitude resulting in the interaction energy being much lower than when the particles are at a more considerable distance apart.

A further study of electrostatic interaction between bipatchy particles at a short-range separation was carried out. A set of results was obtained for the two-body systems as a function of the angle separated by surface-to-surface

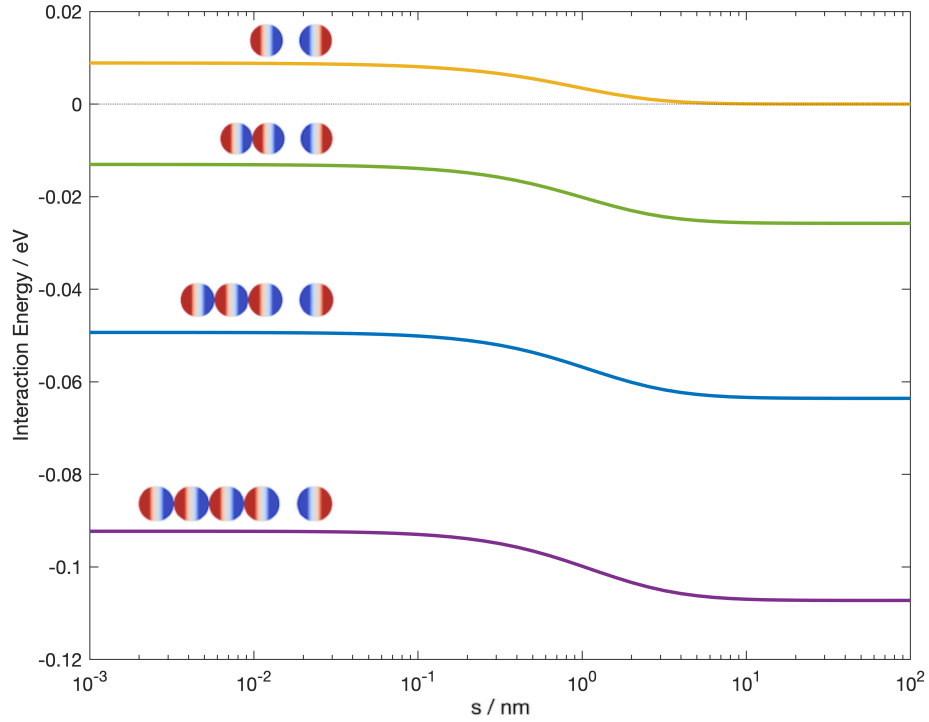


Figure 3.12: Interaction energy as a function of surface-to-surface separation s between bipatchy particles. Patch geometry is defined by $v = 0.8$ and $P = 5$ using equation (3.7); red patch $q = +1e$ and blue patch $q = -1e$. For $k_p = 20$, $k_m = 1$, particles radii $a = 1$ nm.

0.001 nm distance. The interacting spheres have dielectric constant $k_p = 20$, and are placed in a vacuum $k_m = 1$. The effect of changing the patch and particle size as well as the charge ratio was examined.

An interaction energy was measured for two bipatchy particles where one of the bipatchy particles has a fixed radius $a_1 = 1$ nm and the second bipatchy particle increases in size from $a_2 = 1$ nm to $a_2 = 2$ nm and subsequently to $a_2 = 3$ nm. The attraction at zero degrees angle (a stable configuration) between bipatchy particles increases as the particle increases in size (figure 3.14). Also, the attractive regime occurs at a larger surface of the rotating particle as the system becomes more asymmetric. Likewise, when the patch size grows together with the particle's radius, this gives rise to the attraction contribution of the electrostatic energy (appendix A.3). As the size ratio increases to 1 : 3 nm with a patch at its maximum allowable size, the attraction energy dominates at

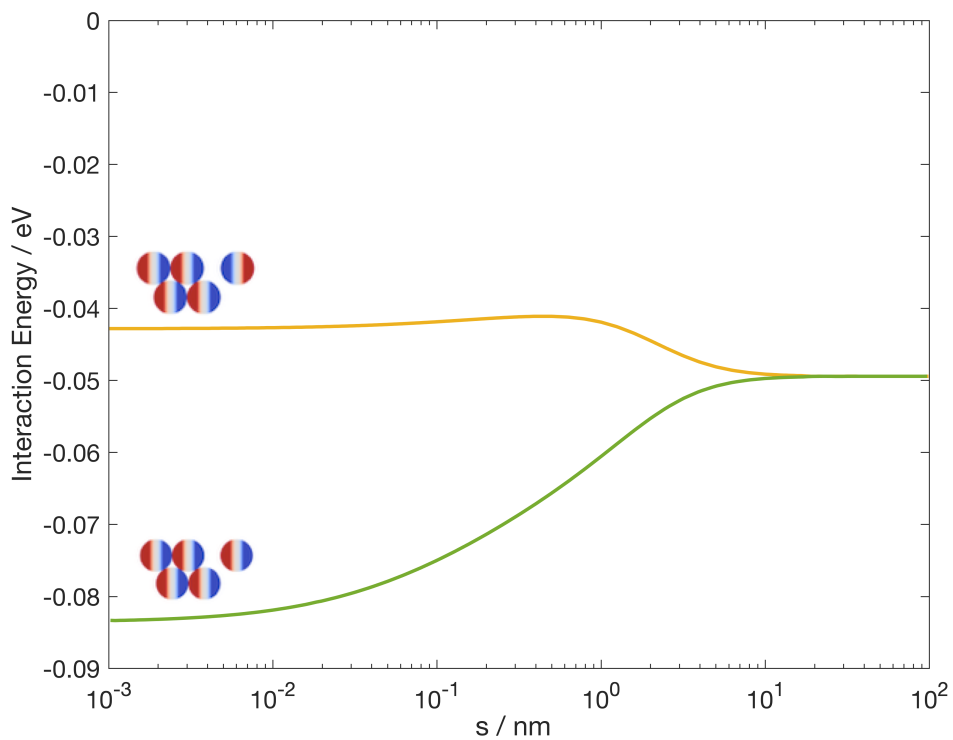


Figure 3.13: Interaction energy as a function of surface-to-surface separation s between bipatchy particles. Patch geometry is defined by $\nu = 0.8$ and $P = 5$ using equation (3.7); red patch $q = +1e$ and blue patch $q = -1e$. For $k_p = 20$, $k_m = 1$; particles radii $a = 1$ nm.

all the rotational angles due to the influence of polarisation of surface charge as shown in appendix A.3 (purple plot).

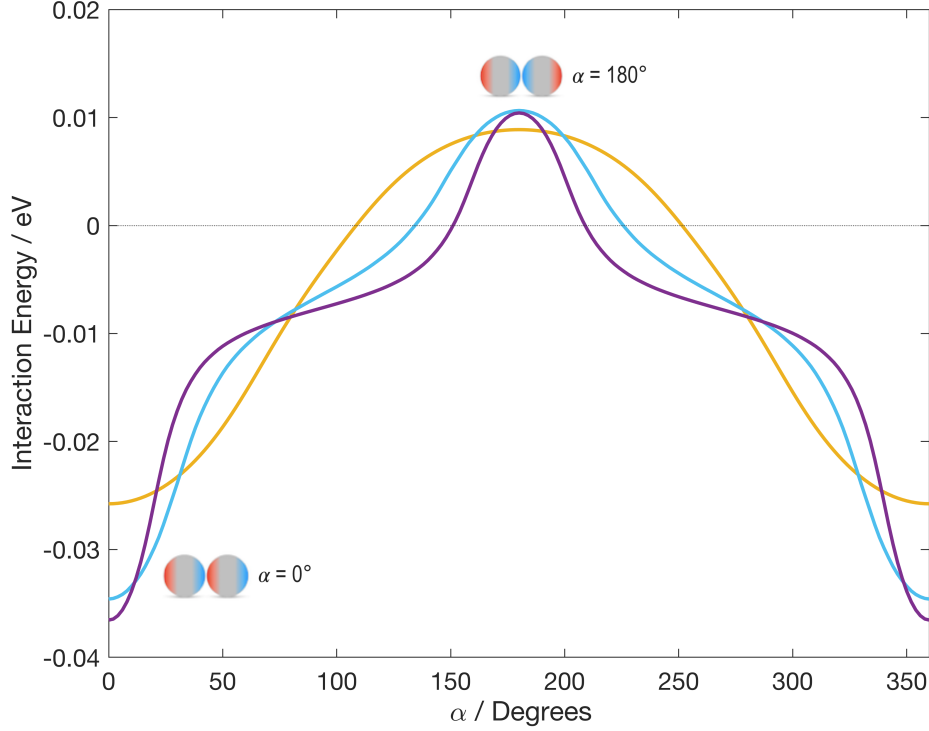


Figure 3.14: Interaction energy as a function of α for the interaction between two bipatchy particles at a fixed surface-to-surface separation $s = 0.001$ nm. Patch geometry is defined by $v = 0.8$ and $P = 5$ using equation (3.7); red patch $q = +1e$ and blue patch $q = -1e$. For $k_p = 20$, $k_m = 1$, $a = 1$ nm and $a_2 = 1$ nm (yellow), $a_2 = 2$ nm (blue), $a_2 = 3$ nm (purple).

Following the investigation of the attraction at a touching point for systems with bipatchy particles' size ratio, further analysis was carried when the charge was altered on a patch. The charge distribution was decreased by the magnitude and density of charge on negatively charged patches of the two bipatchy particles to $q = -0.9e$, while positively charged patches remained with charge $q = +1e$ for all scenarios in figure 3.15. The attractive term of the interaction energy decreases as the charge on a negative patch decreases to $q = -0.9e$ in a configuration of the oppositely charged patches facing each other on the bipatchy particles (blue plots, angle = 0°), when comparing to the system with bipatchy particles possessing symmetrical in terms of charge patches

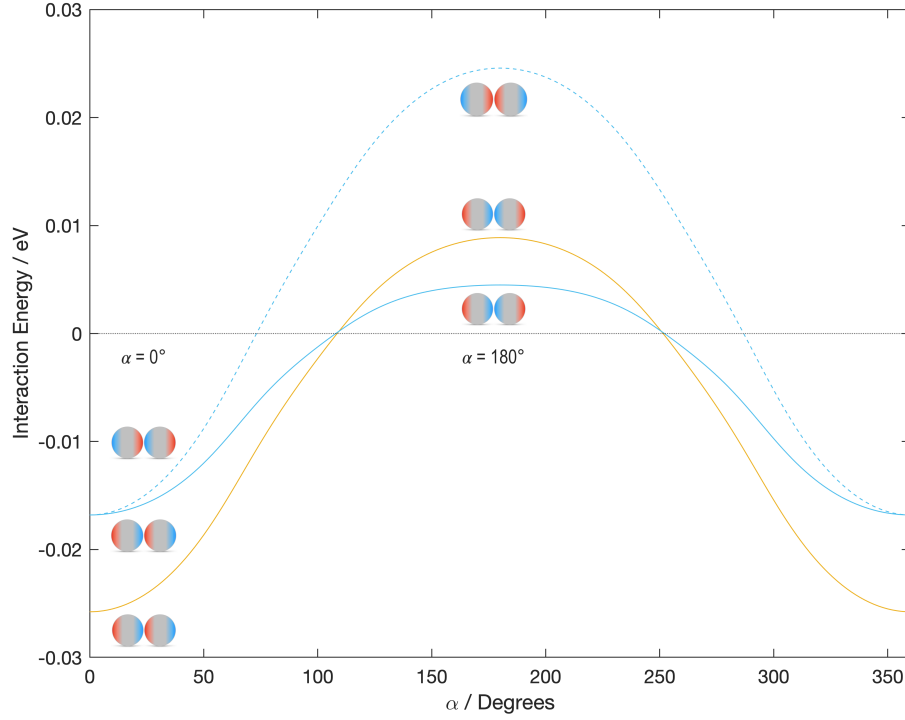


Figure 3.15: Interaction energy as a function of α for the interaction between two bipatchy particles at a fixed surface-to-surface separation $s = 0.001$ nm. For $k_p = 20$, $k_m = 1$; $a_1 = a_2 = 1$ nm. Patch geometry are defined by $v = 0.8$ and $P = 5$ using equation (3.7); $q_1 = +1e$ (red patch) and $q_2 = -1e$ (blue patch) - yellow plot; $q_1 = +1e$ (red patch) and $q_2 = -0.9e$ (blue patch) - blue plots.

(yellow plot, angle = 0°). The repulsive term also decreases for the system with patches possessing charge $q = -0.9e$ and facing each other at the repulsive configuration (blue solid plot, angle = 180°) in comparison to a system with all patches having the same magnitude and density of charge and negative patches are also facing each other (yellow plot, angle = 180°). Oppositely, when two bipatchy particles are set at a configuration that the positively charged patches face each other (angle = 180°) the repulsion rises because the patches that face each other possess a greater magnitude and density of charge (blue dashed plot).

Knowing the predictions for the stability of systems with unequal size patches of oppositely charged bipatchy particles can support future experimental work more relevant. For this analysis, a patch size was altered for both negatively and positively charged patches on two bipatchy particles $a_1 = a_2 = 1$ nm. The

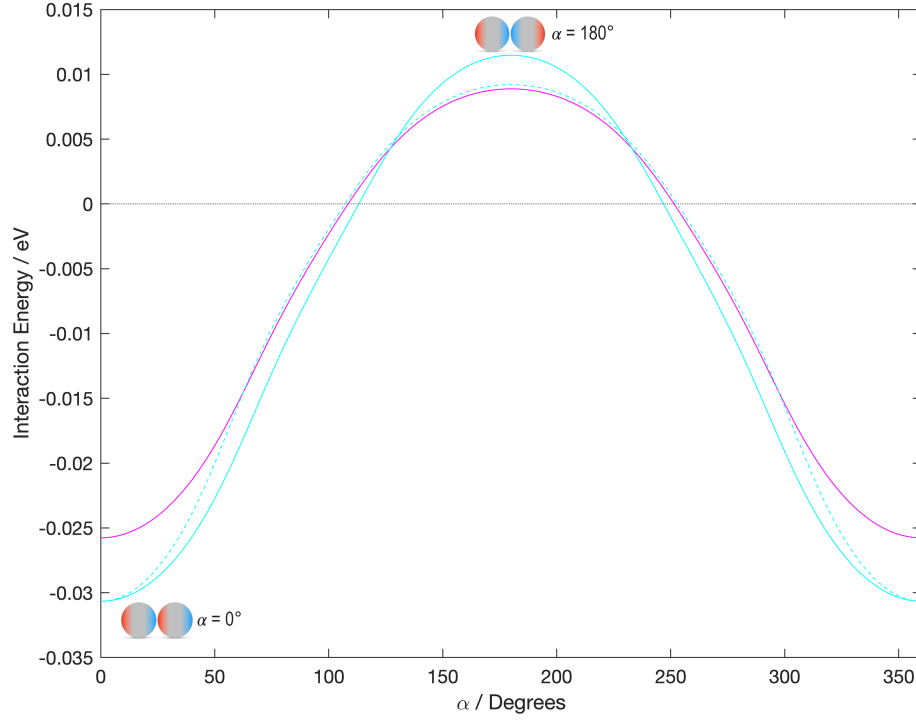


Figure 3.16: Interaction energy as a function of α for the interaction between two bipatchy particles at a fixed surface-to-surface separation $s = 0.001$ nm. For $k_p = 20$, $k_m = 1$; $a_1 = a_2 = 1$ nm; $q_1 = +1e$ (red patch) and $q_2 = -1e$ (blue patch); Patches geometry: $P = 5$; all patches $v = 0.8$ (magenta); positive red patch $v = 0.8$ and negative blue patch $v = 0.7$ (cyan solid line), positive red patch $v = 0.7$ and negative blue patch $v = 0.8$ (cyan dashed line) using equation (3.7).

cyan plots in figure 3.16 show an increase in the attractive term at a stable configuration (angle = 0°) due to the asymmetry of the oppositely charged patches (compared to the scenario of bipatchy particle with equal sized patches - magenta plot, angle = 0°). The slight increase in stability is due to increased surface charge density at the smaller patches, thereby inducing the bond charges on the remaining patches. The repulsive Coulomb term is increased for the bipatchy particles at unstable configuration with smaller patches facing each other (solid cyan plot, angle = 180°) due to a decrease of polarisation of the bound charge. A case of positioning larger in size like-charged patches at repulsive connection leads to a decrease in Coulombic repulsion (cyan dashed plot, angle = 180°) compared to smaller patches facing each other (solid cyan plot, angle = 180°). The observed trend is due to the increase in polarisation of the charge density on the larger patches.

After demonstrating the ability of higher-order Gaussian distribution to model a patch while holding the charge within a patch dimension to a greater limit of the standard deviation of the distribution than normal Gaussian, further modelling is presented. In addition to altering the patch "flatness", the patch size can also be modelled up to a precise value. The following section describes the solution to obtain the desired diameter of a patch.

3.3 Modelling a patch

A higher-order Gaussian distribution compared to a normal Gaussian distribution allows modelling a patch with a fatter top shape. In addition the patch size can be modelled without loss of charge. Having an equation (3.9) for chord length d_c , a specific patch size can be obtained. The equation for a chord is given by the formula:

$$d_c = 2 \cdot r \cdot \sin \cdot \frac{t}{2}. \quad (3.9)$$

In the equation, the variable t represents the central angle in radians (that subtends the arc), and the variable r corresponds to the particle's radius, as illustrated in Figure 3.17.

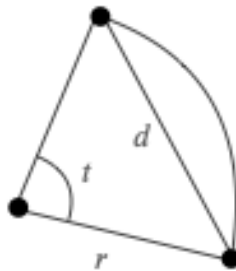


Figure 3.17: Visualisation of variables required for the equation (3.9) for chord length d_c .

The presented work shows the validation of higher-order Gaussian distribution of charge density used as modeling a patch on a particle's surface. A full range of capabilities of the model was demonstrated. The work progresses to explore the electrostatic interaction between oppositely charged inverse bipatchy particles introduced by Mehr et al.[1].

Chapter 4

Computational modelling of oppositely charged inverse bipatchy particles

The work in this chapter specifically focuses on the prediction of results for the system discussed in Mehr et al.[1]. The following report presents more satisfying results with a two-body approach where a patch is modelled by a distribution of charge on a particle's surface with an exact size given in the experimental results[1].

4.1 Comparison of charge distribution methods

After validating the accuracy of the implemented higher-order Gaussian distribution of charge, this work attempted to compare the higher-order and uniform distribution of charge.

In 2020 Mehr et al.[1] presented a study of self-assembly behaviour of oppositely charged inverse bipatchy microcolloids and modelling the patches by a uniform distribution of charge on the smaller spheres in the analysed systems. In the

experimental section, the patches were reported to have a size of 2.33 ± 0.16 and $2.4 \pm 0.2 \mu\text{m}$ for polyethylenimine (PEI) and poly(methyl vinyl ether-alt-maleic acid) (PMVEMA) patches, respectively. In order to recreate the patches' geometry, a higher-order Gaussian distribution implementation was used to model patchy particles. The remaining required variables were taken from Table 3 in Mehr et al.[1]. After presenting numerical tests of higher-order distribution of charge in the form of a patch on a particle's surface and presenting a variety of trends afterwards, this report attempts to compare the results published by Mehr et al.[1] with the results obtained by implementing higher-order Gaussian distribution. Mono-patchy and bi-patchy particles were computationally modelled to investigate the interaction energy between colloidal particles using many-body solution.

Looking at figure 4.1 and figure 4.2 - both figures show interaction energy between bipatchy-bipatchy and bipatchy-monopatchy particles as a function of surface-to-surface separation s . The solid lines in both figures show the results from "Self-Assembly Behavior of Oppositely Charged Inverse Bi-patchy Microcolloids" article where a bipatchy particle is represented by a mother particle and two smaller particles located on the opposite pole imitating the patches. The dashed lines in figure 4.1 and 4.2 are results generated by higher-order Gaussian distribution, which allowed to place patches on the spheres, thus, creating a two-body system.

Both methods show the same trends for the interaction between bipatchy particles in figure 4.1. However, the electrostatic interactions predicted with the uniform distribution of charge (the solid lines) were a lot weaker in comparison to the results obtained with higher-order Gaussian distribution (the dashed lines). The results for the two-body system show that the attraction energy is much more substantial for inner patches with opposite charge signs. Also, the repulsive interactions are much stronger for inner patches with the same charge signs. Although, the results will differ as those two methods have different forms

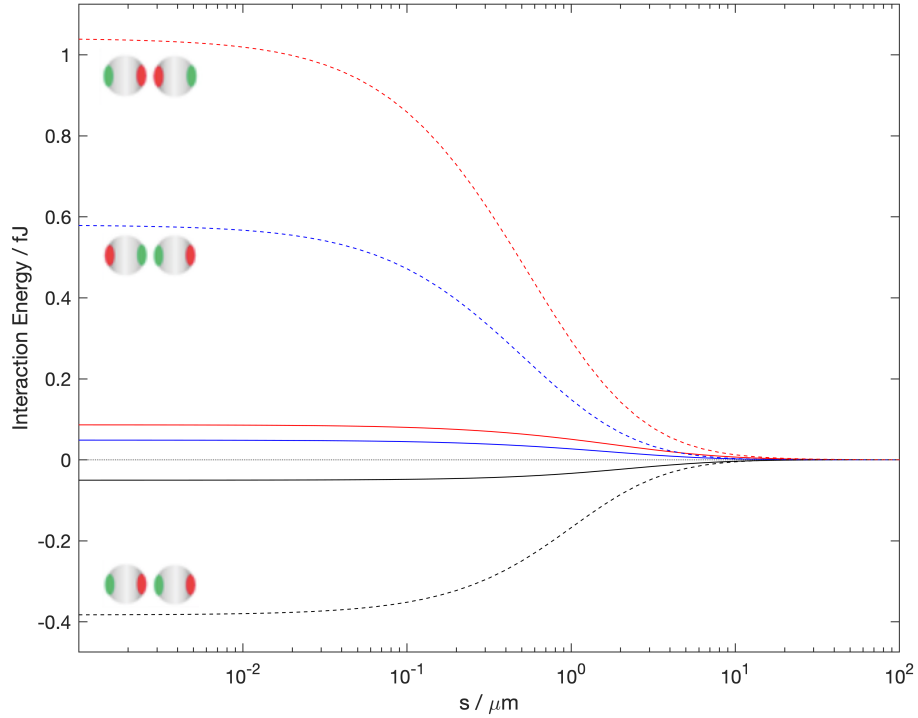


Figure 4.1: Interaction energy as a function of surface-to-surface separation s . Recreation of results from Mehr et al. (figure 5a) [1] - solid lines. Interaction between bi-patchy particles with variables set to $P = 5$ and $v/a_{1,2} = 0.27$ for PEI patch and $v/a_{1,2} = 0.28$ for PMVEMA patch (using equation (3.7)) to recreate the patch's size from the experimental results in Mehr et al.[1]. Negatively charged patch PMVEMA $q = -0.923$ fC (red colour) and positively charged patch PEI $q = +0.734$ fC (green colour).

of distributing the charge. Nonetheless, the higher-order Gaussian distribution allows modelling a patch with an exact patch size reported in experimental results.

Figure 4.2 displays also the same trends for both methods. The repulsive interaction increases in magnitude at short separation for the two-body systems with a higher-order charge distribution. In addition, the higher-order distribution gives a lower energy minimum. For the higher-order Gaussian distribution, when the outer patches have the same sign (red and blue dashed plots), the interaction energy becomes more repulsive when there is less charge density placed on the outer patches, which is the opposite to the results generated by the uniform distribution of charge (red and blue solid plots). Also, the experi-

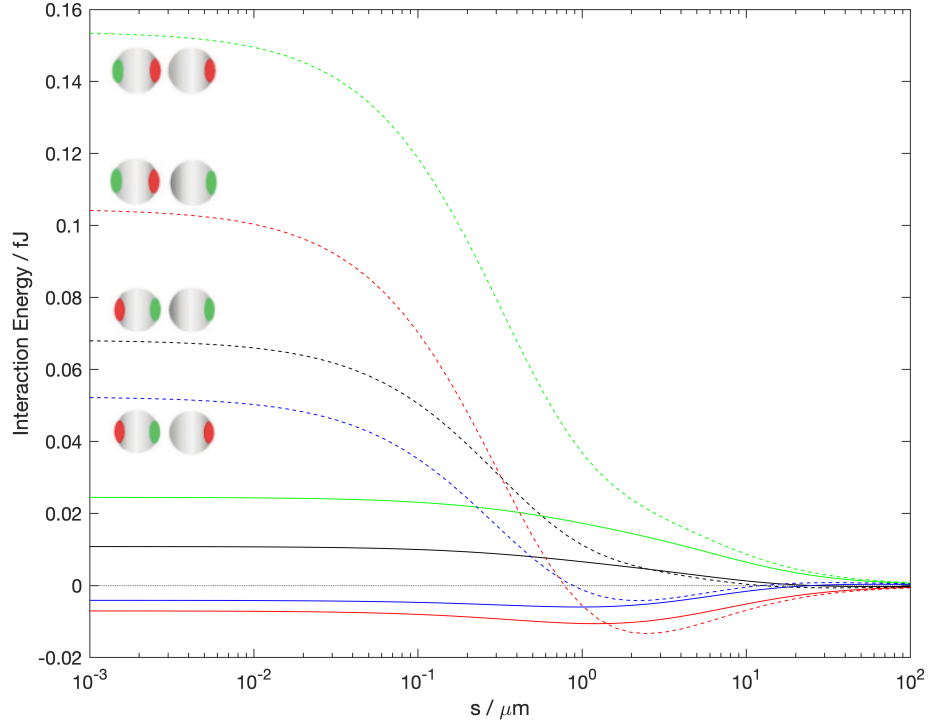


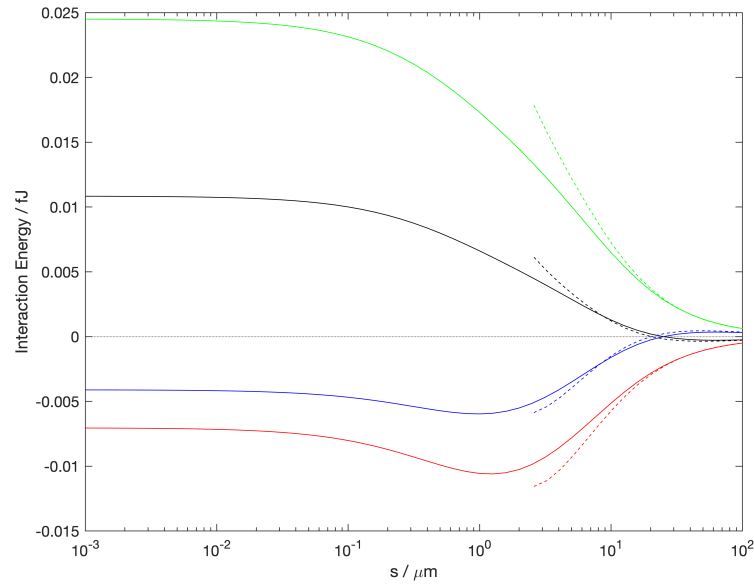
Figure 4.2: Interaction energy as a function of surface-to-surface separation distance between particles. Recreation of results from Mehr et al. (figure 5b) - solid lines. Interaction between bi-patchy and mono-patchy particle with variables set to $P = 5$ and $v/a_{1,2} = 0.27$ for PEI patch and $v/a_{1,2} = 0.28$ for PMVEMA patch (using equation (3.7)) to recreate the patch's size from the experimental results in Mehr et al. Negatively charged patch PMVEMA $q = -0.923$ fC (red colour) and positively charged patch PEI $q = +0.734$ fC (green colour).

mental data figure 1.3 (figure 2c from Mehr et al.[1]) exhibits larger fractions of interaction between MF neutral particle and PEI patch (green colour), as predicted with a higher-order distribution of charge. However, figure 1.3 (figure 2c from Mehr et al.[1]) does not show exactly if the interacting particles were monopatchy or consisted of two patches or neutral MF particle. The difference in magnitude of the interaction energy between both methods might be due to the difference in surface-to-surface separation between the central MF particles.

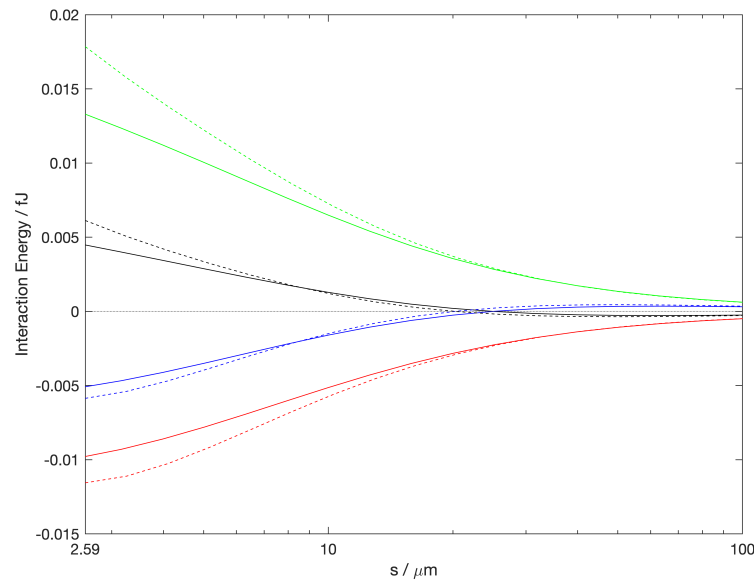
The conclusion leads to a comparison of interaction energies between two methods of distributing a charge when the MF mother particles are at the same surface-to-surface separation distance. In order to match the separation between MF particles in higher-order distribution (two-body system) to the

uniform distribution of charge (five-body system), an additional distance needs to be added equal to the diameter of the smaller sphere that represents a patch for the uniform distribution of charge. Figure 4.3 displays the results between uniform and higher-order distribution when MF particles for higher-order distribution only approach each other as close as the model allows for uniform distribution. Nevertheless, if one treats the shortest separations in the two-body system as equal to the separation in the five-body system, one should present the results in a parallel manner where the shortest separations for the two methods are equivalent. The magnitude of interaction energy at the shortest separation for both methods turns out to be similar, but the trends are now contrasting (solid lines separation s ranges from 0.001 to 100 μm and dashed lines the closest separation starts from 5.181 μm and rises to 100 μm). However, in nature, the particles would approach each other at a closer distance than 2.591 μm . Also, for a case of the shortest surface-to-surface separation $s = 5.181 \mu\text{m}$ (red and blue dashed plots, figure 4.3a), if one compares the interaction energies for systems with identical outer patches generated by higher-order distribution, the results show disagreement for the experimental data of PEI-MF and PMVEMA-MF in figure 1.3 - PEI-MF orientation was formed more often than PMVEMA-MF pair (as the dashed red and blue plots in figure 4.2 show an agreement with the experimental data - figure 1.3).

Mehr et al.[1] also studied the rotational barrier for oppositely bipatchy microparticles with oppositely charged patches. Comparisons were carried out to examine the behaviour of bipatchy particles at a fixed separation and rotation of one of the bipatchy particles in a considered system - figure 4.4. From figure 4.5, the results obtained by modelling a two-body system with patches printed on the MF spheres show the same trends as the work produced by Mehr et al.[1]. Following the previous assumption, a comparison was made to match the shortest surface-to-surface separation between the six-body system and the two-body system (where the patches placed on the sphere) - for



(a)



(b)

Figure 4.3: Interaction energy as a function of surface-to-surface separation distance between particles. Interaction between five-body system with uniformly distributed charge on each particle – recreation of results from Small by Mehr et al. (solid lines). Interaction between bi-patchy and mono-patchy particles with variables set to be $P = 5$ and $v/a_{1,2} = 0.27$ for PEI patch and $v/a_{1,2} = 0.28$ for PMVEMA patch to recreate the patch's size from the experimental results. Negatively charged patch PMVEMA $q = -0.923$ fC (red colour) and positively charged patch PEI $q = +0.734$ fC (green colour); figure b shows interaction energy as a function of surface-to-surface separation distance between particles only from the distance $s = 5.181$ μm .

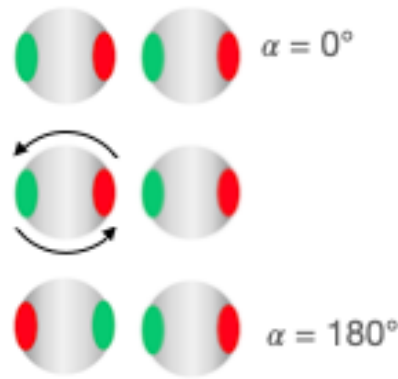
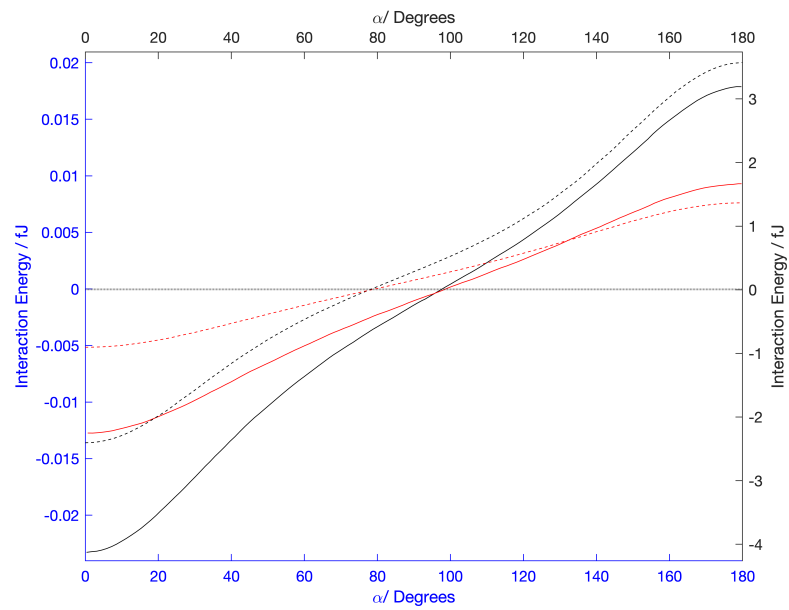


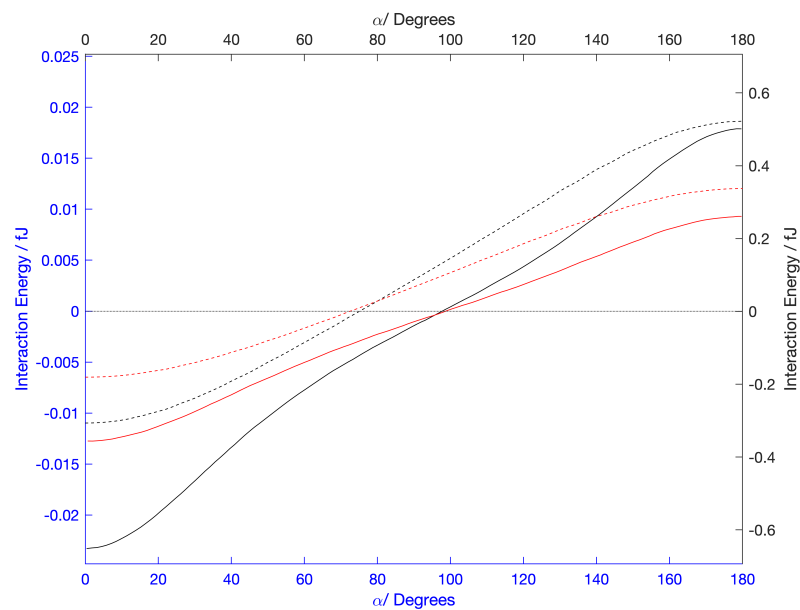
Figure 4.4: The re-orientation of a bi-patchy pair from a stable PMVEMA-PEI configuration ($\alpha = 0^\circ$) to a repulsive PEI-PEI connection ($\alpha = 180^\circ$).

both systems the shortest surface-to-surface separation distances s are $4 \mu\text{m}$ (red) and $2 \mu\text{m}$ (black) - figure 4.5a. In addition, a set of calculations were made for systems matching the separation distance of the MF central particles (additional separation was added of two smaller spheres that represent the patches in the uniform distribution of charge) - figure 4.5b. In both cases the plots have a remarkably similar shape to the data generated with uniform distribution. Similar trends might indicate that the redistribution of surface charge and polarisation of charge density during the rotation of a bipatchy particle is comparable. The attraction energy diminishes as the like-charged patches approach each other, and the Coulomb energy barrier decreases with increasing the separation - identical with the results published by Mehr et al.[1]. However, for the former, the interaction energy magnifies 100 times for the two-body system (figure 4.5a). Nevertheless, the separation is not constant for the rotation of the bipatchy particle in the six-body model (perpendicular reorientation between the bipatchy particles increases the separation by the size of the smaller sphere), unlike for the two-body system. Therefore, the results corresponding to higher-order Gaussian distribution most likely resemble the trends of the interaction energy that happen between polymer bi-patchy particles.

The above computational analysis of oppositely charged inverse bipatchy parti-



(a)



(b)

Figure 4.5: The calculated rotational barrier (in fJ) for re-orientation of a bi-patchy pair from a repulsive PEI-PEI connection ($\alpha = 180^\circ$) to a stable PMVEMA-PEI configuration ($\alpha = 0^\circ$) at two surface-to-surface separation distances: $2 \mu\text{m}$ (black), and $4 \mu\text{m}$ (red). The particle rotates around stationary particle facing the stationary particle with PEI patch. The calculated rotational barrier (in fJ) for re-orientation of a bi-patchy pair from a repulsive PEI-PEI connection ($\alpha = 180^\circ$) to a stable PMVEMA-PEI configuration ($\alpha = 0^\circ$) at two surface-to-surface separation distances: $7.18 \mu\text{m}$ (black), and $9.18 \mu\text{m}$ (red). The rotating particle remains at fixed position.

cles indicated that the magnitude of interaction energy differs from the initial computation presented by Mehr et al.[1]. Although the initial results do not vary significantly, the results given in this report present more accurate values for the interaction energies.

Chapter 5

Conclusions and Future Work

This report manifests the implementation of normal Gaussian and higher-order Gaussian method of modelling patchy particles. An extension of work on modelling bipatchy particles may be conducted focusing on more complex systems and dynamic simulations.

Throughout this research, another method to model patchy particles was tested - overlapping spheres. A patchy particle is represented by two overlapping spheres. The overlapping method is an extension of the uniform approach. A three-body system was used to investigate the amount of charge placed on an overlapping sphere that possesses a charge. The first sphere is set to be neutrally charged (grey sphere on the the bottom visualisation in figure 5.1), the overlapping sphere is positively charged $q = +1fC$ (red sphere) and the charge of the third particle is equal to $q = -1fC$ (blue sphere). The first and second sphere intersected producing positively charged patch; the third particle remained with uniformly distributed charge on the particle's surface $q = -1fC$. The patch's size was set to $0.1 \mu m$, whereas the larger particles have radius equal to $a_{1,2} = 2.59\mu m$. An anomaly can be seen in the results for the particles at a shorter distance. The interaction energy increases by an order of magnitude compared to the methods outlined in section 3.1.

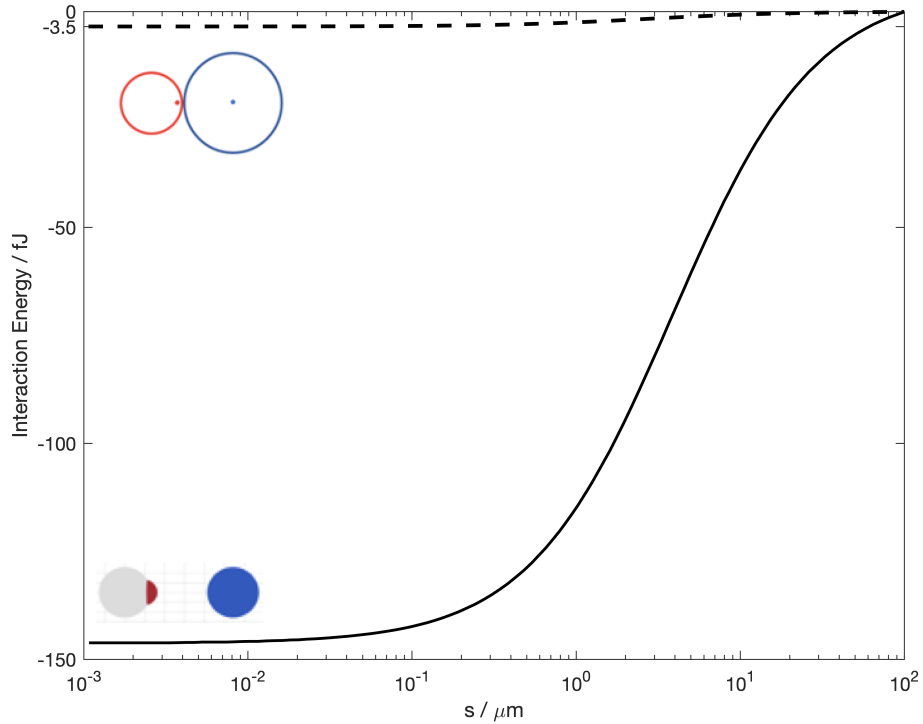


Figure 5.1: Interaction energy as a function of surface-to-surface separation s for overlapping particles method (solid), and point charges using the potential energy equation 3.8 (dashed).

The testing against Coulomb’s law showed that the model does not give an adequate magnitude of charge distributed on a small patch. This development of the method would give an alternative way to represent patchy particles.

The ability to model a patch of the desired size has improved the results published in 2020 by Mehr et al.[1]. However, higher-order Gaussian distribution is designed for two-dimensional surfaces. Thus, developing a method that distributes the charge density on curved surfaces would be even more appropriate. Kent distribution may be more adequate for spherical objects, albeit it is a much more complex function[40].

Bibliography

- [1] F. N. Mehr, D. Grigoriev, R. Heaton, J. Baptiste, A. J. Stace, N. Pureskiy, E. Besley, and A. Böker. Self-Assembly Behavior of Oppositely Charged Inverse Bipatchy Microcolloids. *Small*, 16(14):2000442, apr 2020. ISSN 1613-6810. doi: 10.1002/sml.202000442.
- [2] B. Bharti and O. D. Velev. Assembly of reconfigurable colloidal structures by multidirectional field-induced interactions. *Langmuir*, 31(29):7897–7908, 2015.
- [3] E. B. Lindgren, A. J. Stace, E. Polack, Y. Maday, B. Stamm, and E. Besley. An integral equation approach to calculate electrostatic interactions in many-body dielectric systems. *J. Comput. Phys.*, 371:712–731, 2018.
- [4] J. Yan, M. Han, J. Zhang, C. Xu, E. Luijten, and S. Granick. Reconfiguring active particles by electrostatic imbalance. *Nat. Mater.*, 15(10):1095–1099, 2016.
- [5] Y. [Yufeng] Wang, Y. Wang, D. R. Breed, V. N. Manoharan, L. Feng, A. D. Hollingsworth, M. Weck, and D. J. Pine. Colloids with valence and specific directional bonding. *Nature*, 491(7422):51–55, 2012.
- [6] Z. Zhang and S. C. Glotzer. Self-assembly of patchy particles. *Nano lett.*, 4(8):1407–1413, 2004.
- [7] J. Baptiste, C. Williamson, J. Fox, A. J. Stace, M. Hassan, S. Braun, B. Stamm, I. Mann, and E. Besley. The influence of surface charge on the coalescence of ice and dust particles in the mesosphere and lower thermosphere. *Atmos. Chem. Phys.*, 21(11):8735–8745, 2021.
- [8] E. B. Lindgren, B. Stamm, H. Chan, Y. Maday, A. J. Stace, and E. Besley. The effect of like-charge attraction on aerosol growth in the atmosphere of titan. *Icarus*, 291:245–253, 2017.
- [9] H. Zhou and X. Pang. Electrostatic interactions in protein structure, folding, binding, and condensation. *Chem. Rev.*, 118(4):1691–1741, 2018.
- [10] A. G. Cherstvy. Electrostatic interactions in biological dna-related systems. *Phys. Chem. Chem. Phys.*, 13(21):9942–9968, 2011.
- [11] J. Hees, A. Kriele, and O. A. Williams. Electrostatic self-assembly of diamond nanoparticles. *Chem. Phys. Lett.*, 509(1-3):12–15, 2011.

- [12] E. V. Shevchenko, D. V. Talapin, N. A. Kotov, S. O'Brien, and C. B. Murray. Structural diversity in binary nanoparticle superlattices. *Nature*, 439(7072):55–59, 2006.
- [13] B. Abécassis. Three-dimensional self assembly of semiconducting colloidal nanocrystals: from fundamental forces to collective optical properties. *ChemPhysChem*, 17(5):618–631, 2016.
- [14] X. Liang, R. Dong, and J. C. Ho. Self-assembly of colloidal spheres toward fabrication of hierarchical and periodic nanostructures for technological applications. *Adv. Mater. Technol.*, 4(3):1800541, 2019.
- [15] V. Liljeström, C. Chen, P. Dommersnes, J. O. Fossum, and A. H. Gröschel. Active structuring of colloids through field-driven self-assembly. *Curr. Opin. Colloid Interface Sci.*, 40:25–41, 2019.
- [16] P. R. Sajjanlal, T. S. Sreeprasad, A. K. Samal, and T. Pradeep. Anisotropic nanomaterials: structure, growth, assembly, and functions. *Nano Rev.*, 2(1):5883, 2011.
- [17] J. Du and R. K. O'Reilly. Anisotropic particles with patchy, multicompartment and janus architectures: preparation and application. *Chem. Soc. Rev.*, 40(5):2402–2416, 2011.
- [18] N. Patra and A. V. Tkachenko. Programmable self-assembly of diamond polymorphs from chromatic patchy particles. *Phys. Rev. E*, 98(3):032611, 2018.
- [19] Z. Zhang, A. S. Keys, T. Chen, and S. C. Glotzer. Self-assembly of patchy particles into diamond structures through molecular mimicry. *Langmuir*, 21(25):11547–11551, 2005.
- [20] Y. Wang, A. D. Hollingsworth, S. K. Yang, S. Patel, D. J. Pine, and M. Weck. Patchy particle self-assembly via metal coordination. *J. Am. Chem. Soc.*, 135(38):14064–14067, 2013.
- [21] Y. Lu, J. Lin, L. Wang, L. Zhang, and C. Cai. Self-assembly of copolymer micelles: higher-level assembly for constructing hierarchical structure. *Chem. Rev.*, 120(9):4111–4140, 2020.
- [22] B. Luo, J. W. Smith, Z. Wu, J. Kim, Z. Ou, and Q. Chen. Polymerization-like co-assembly of silver nanoplates and patchy spheres. *ACS nano*, 11(8):7626–7633, 2017.
- [23] M. R. U. AFM. Patchy particles. *Nat. Mater.*, 22:977–984, 2004.
- [24] Q. Chen and S. Granick. From patchy particles to open lattices. *Synthesis and self-assembly of multiblock janus particles*, page 109, 2012.
- [25] C. K. Wong, F. Chen, A. Walther, and M. H. Stenzel. Bioactive patchy nanoparticles with compartmentalized cargoes for simultaneous and trackable delivery. *Angew. Chem.*, 131(22):7413–7418, 2019.

- [26] L. Tran, S. Lesieur, and V. Faivre. Janus nanoparticles: materials, preparation and recent advances in drug delivery. *Expert. Opin. Drug Deliv.*, 11(7):1061–1074, 2014.
- [27] A. B. Pawar and I. Kretzschmar. Fabrication, assembly, and application of patchy particles. *Macromol. Rapid Commun.*, 31(2):150–168, 2010.
- [28] F. N. Mehr, D. Grigoriev, N. Pureskiy, and A. Böker. Mono-patchy zwitterionic microcolloids as building blocks for ph-controlled self-assembly. *Soft matter*, 15(11):2430–2438, 2019.
- [29] J. Wong, Y. Lin, P. C. L. Kwok, V. Niemelä, J. Crapper, and H. Chan. Measuring bipolar charge and mass distributions of powder aerosols by a novel tool (bolar). *Mol. Pharm.*, 12(9):3433–3440, 2015.
- [30] A. Jaworek, A. Krupa, and T. Czech. Modern electrostatic devices and methods for exhaust gas cleaning: A brief review. *J Electrostat.*, 65(3):133–155, 2007.
- [31] J. Baptiste, C. Pang, D. Prime, E. Besley, M. Hamilton, and A. J. Stace. Charged particle dynamics in dry powder inhalers: Evidence of particle scavenging. in preparation.
- [32] L. Holbrook, M. Hindle, and P. W. Longest. Generating charged pharmaceutical aerosols intended to improve targeted drug delivery in ventilated infants. *J. Aerosol Sci.*, 88:35–47, 2015.
- [33] M. Horányi. Charged dust dynamics in the solar system. *Annu. Rev. Astron. Astrophys.*, 34(1):383–418, 1996.
- [34] E. Bichoutskaia, A. L. Boatwright, A. Khachatourian, and A. J. Stace. Electrostatic analysis of the interactions between charged particles of dielectric materials. *J. Chem. Phys.*, 133(2):1–10, 2010. ISSN 00219606. doi: 10.1063/1.3457157.
- [35] W. S. Czarnecki and L. B. Schein. The contribution of the electrostatic proximity force to atomic force microscopy with insulators. *Phys. Lett. A*, 339(1-2):145–151, 2005.
- [36] R. Messina. Image charges in spherical geometry: Application to colloidal systems. *J. Chem. Phys.*, 117(24):11062–11074, 2002.
- [37] P. Linse. Electrostatics in the presence of spherical dielectric discontinuities. *J. Chem. Phys.*, 128(21):214505, 2008.
- [38] A. Khachatourian, H. Chan, A. J. Stace, and E. Bichoutskaia. Electrostatic force between a charged sphere and a planar surface: A general solution for dielectric materials. *J. Chem. Phys.*, 140(7):074107, 2014.
- [39] A. V. Filippov, X. Chen, C. Harris, A. J. Stace, and E. Besley. Interaction between particles with inhomogeneous surface charge distributions: Revisiting the coulomb fission of dication molecular clusters. *J. Chem. Phys.*, 151(15):154113, 2019.

- [40] J. T. Kent. The fisher-bingham distribution on the sphere. *J R Stat Soc Series B (Methodological)*, 44(1):71–80, 1982. ISSN 00359246. URL <http://www.jstor.org/stable/2984712>.
- [41] O. I. Obolensky, T. P. Doerr, A. Y. Ogurtsov, and Y. Yu. Can dielectric spheres accurately model atomic-scale interactions? *EPL EPL-EUROPHYS. LETT.*, 116(2):24003, 2016.
- [42] J. al Mitroy, M. S. Safronova, and C. W. Clark. Theory and applications of atomic and ionic polarizabilities. *J. Phys. B: At., Mol. Opt. Phys.*, 43(20):202001, 2010.
- [43] L. Hamonou and A. Hibbert. Static and dynamic polarizabilities of mg-like ions. *J. Phys. B: At., Mol. Opt. Phys.*, 41(24):245004, 2008.
- [44] L. Hamonou and A. Hibbert. Static and dynamic polarizabilities of na-like ions. *J. Phys. B: At., Mol. Opt. Phys.*, 40(18):3555, 2007.
- [45] K. E. Laidig and R. F. W. Bader. Properties of atoms in molecules: Atomic polarizabilities. *J. Chem. Phys.*, 93(10):7213–7224, 1990.
- [46] N. Reshetnikov, L. J. Curtis, M. S. Brown, and R. E. Irving. Determination of polarizabilities and lifetimes for the mg, zn, cd and hg isoelectronic sequences. *Phys. Scr.*, 77(1):015301, 2007.
- [47] E. Guan, J. Ciston, S. R. Bare, R. C. Runnebaum, A. Katz, A. Kulkarni, C. X. Kronawitter, and B. C. Gates. Supported metal pair-site catalysts. *ACS Catal.*, 10(16):9065–9085, 2020.
- [48] D. J. Barlow and J. M. Thornton. Ion-pairs in proteins. *J. Mol. Biol.*, 168(4):867–885, 1983.

Appendix A

Supporting results

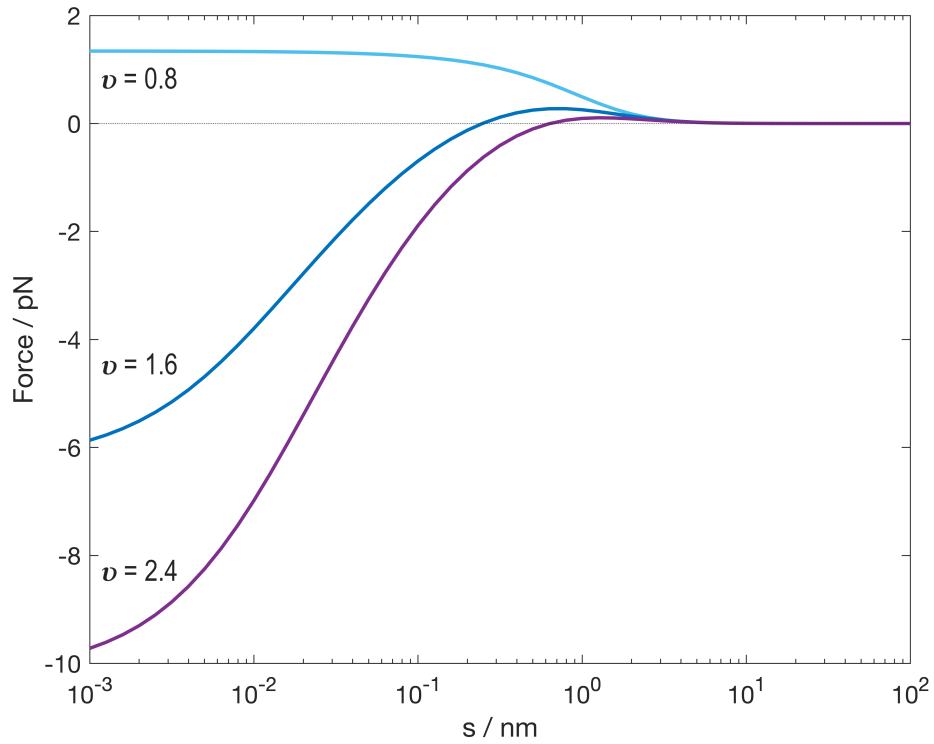


Figure A.1: *Electrostatic force as a function of surface-to-surface separation s between two bipatchy particles (figure 3.7). For $a_1 = 1$ nm, where $\nu = 0.8$, $P = 5$; $k_p = 20$; $k_m = 1$. The patches increase in size along with the particle's size $a_2 = 1$ nm (light blue), $\nu = 0.8$ and $P = 5$; $a_2 = 2$ nm (dark blue), $\nu = 1.6$ and $P = 5$; $a_2 = 3$ nm (purple), $\nu = 2.4$ and $P = 5$ using equation (3.7).*

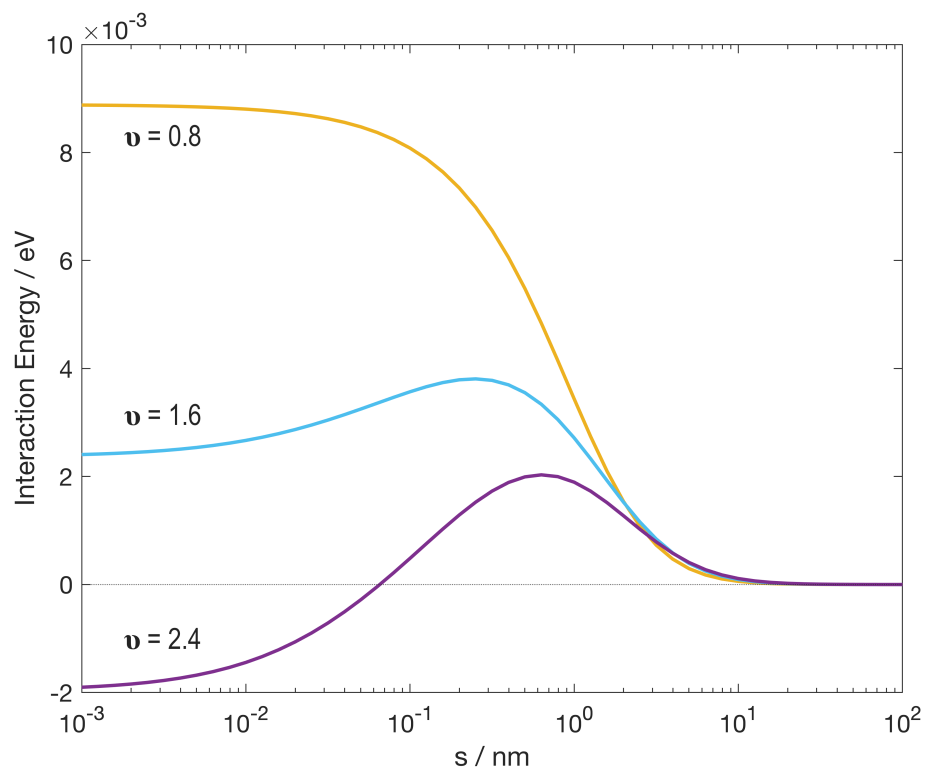


Figure A.2: Interaction energy as a function of surface-to-surface separation s between two bipatchy particles (figure 3.7). For $a_1 = 1$ nm, where $v = 0.8$, $P = 5$; $k_p = 20$; $k_m = 1$. The patches increase in size along with the particle's size $a_2 = 1$ nm (yellow), $v = 0.8$ and $P = 5$; $a_2 = 2$ nm (blue), $v = 1.6$ and $P = 5$; $a_2 = 3$ nm (purple), $v = 2.4$ and $P = 5$ using equation (3.7).

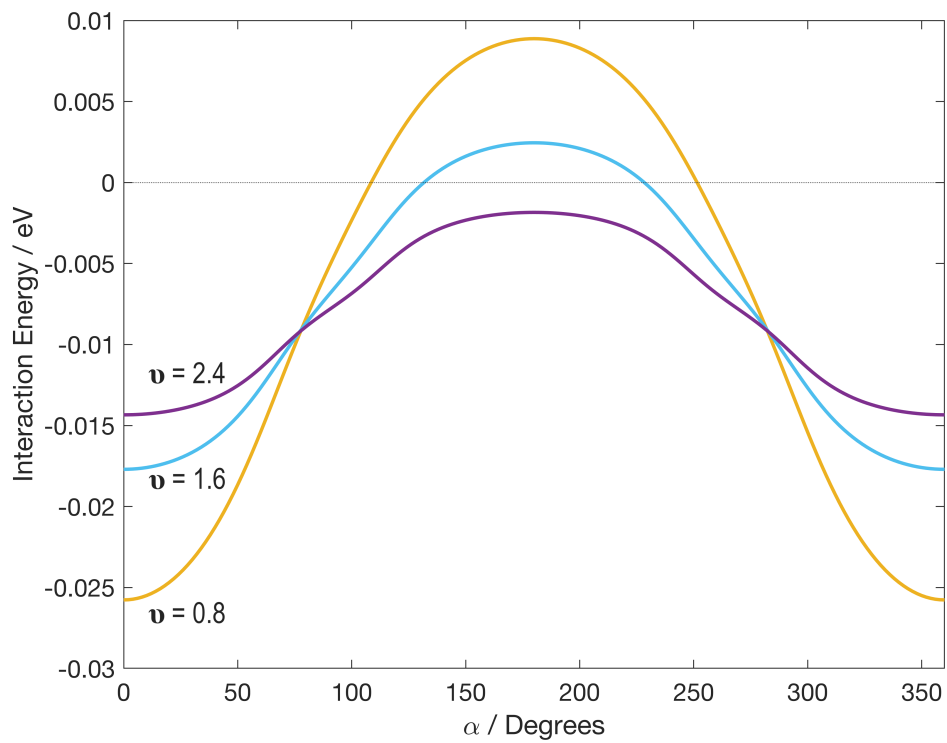


Figure A.3: Interaction energy as a function of surface-to-surface separation s between two bipatchy particles (figure 3.7). For $a_1 = 1$ nm, where $v = 0.8$, $P = 5$; $k_p = 20$; $k_m = 1$. The patches increase in size along with the particle's size $a_2 = 1$ nm (yellow), $v = 0.8$ and $P = 5$; $a_2 = 2$ nm (blue), $v = 1.6$ and $P = 5$; $a_2 = 3$ nm (purple), $v = 2.4$ and $P = 5$ using equation (3.7).

Appendix B

Atomic scale modelling using dielectric spheres

The work showed in this section attempted to investigate the ability of the classical model (introduced in section 2.3) to calculate the polarisation effect with the accuracy of quantum calculations. The high-level calculations were performed using several quantum mechanical methods such as second-order Møller-Plesset perturbation theory (MP2), Density-functional theory (DFT) and Coupled-Cluster with single-double and perturbative triples (CCSD(T)) approximation.

The environment of an electric field can influence dielectric material to change in two different ways. The first effect is deformation of electron shell. The latter is bond distortion. An additional dipole moment is proportional to the applied electric field, and this relationship is described as atomic polarisability α . The Clausius-Mossotti formula describes the relationship between the dielectric constant k (relative permittivity, ϵ_r) and the combination of atomic polarisability α and number of molecules per unit of volume N being expressed as:

$$\left(\frac{k-1}{k+2}\right) = \frac{N\alpha}{3\epsilon_0}, \quad (\text{B.1})$$

where k is the dielectric constant (ϵ/ϵ_0) and ϵ_0 is the permittivity of free space.

Physical processes taking place on the microscale are mainly computed by using the quantum mechanical level of calculations. Calculations with quantum mechanical methods demonstrate the accuracy of the results of a system and can be computationally costly with the increase of the system complexity. The classical models often do not provide the accuracy of expected results but lower the computational cost. Classical models often are a more suitable approach when solving macroscopic systems. Hence, computing quantum scale problems using the classical approach remains a unique challenge. In this section, the work attempted to model atomic-sized systems with quantum-level accuracy. The method treats spheres at atomic detail to calculate the ion-ion and ion-neutral particle systems of aluminium atom. The numerical solution to calculate polarisation portion of the energy in this section is based on a formalism of an arbitrary number of dielectric spherical particles with surface charge distribution of arbitrary size, dielectric constant and charge. The dielectric particles in this problem are embedded in vacuum. In order to calculate the polarisation effect via using the classical model, a number of parameters of the dielectric particles are required. Each particle that represents an atom in the system needs to have its dielectric constant k_p and radius a . The quantum theory does not explicitly specify a dielectric constant value for individual atoms. Hence, both parameters are related with the concept of atomic polarisability α [41]. The atomic polarisability defines the ratio between the applied electric field and induced dipole moment of an atom. An extensive experimental and theoretical data have been critically evaluated, compared and analysed for individual atoms and ions[42–46].

In 2016 Obolensky et al.[41] proposed a mathematical expression that correlates the radius of an atom of interest and its dielectric constant for a considered

polarisability α of dielectric sphere, given by:

$$\alpha = \frac{k_p - 1}{k_p + 2} a^3, \quad (\text{B.2})$$

where the radius must be $(\alpha)^{1/3}$ to agree to the following condition $k_p > 1$.

To extract the polarisation portion from the quantum level results Obolensky et al. proposed an expression for total energy \mathcal{E} of two atoms or ions A and B separated at a sufficiently large distance L , given by:

$$\mathcal{E} = \mathcal{E}_A + \mathcal{E}_B + \frac{q_A q_B}{L} + U(L), \quad (\text{B.3})$$

where A and B portions of the total energy are the self energies of the considered atoms/ions, possessing the charges q_A and q_B . The term $U(L)$ corresponds to the polarisation portion of the total interaction energy.

Figure B.1 compares the values of the polarisation part of interaction energy $U(L)$ between $\text{Al}^+ - \text{Al}^+$ pair of ions generated by using quantum mechanical methods and the classical approach (described in section 2.3). The results obtained by using classical model with parameters of dielectric particles equal to $a_1 = a_2 = 2\text{\AA}$ and $k_p = 3.52$ with chosen scalar a_0^3 equal to 24.65[41] (green) accurately agrees with the CCSD(T)/aug-cc-pVTZ level of theory (black). Also, dielectric particle pair of radius $a_1 = a_2 = 2.49\text{\AA}$ and dielectric constant $k_p = 1.915$ for 24.4 a_0^3 [41] (red) matches the values from CCSD(T)/aug-cc-pVTZ calculations. Similarly, results of a system of dielectric particles having radius $a_1 = a_2 = 1.54\text{\AA}$ and $k_p = 154.96$ for 24.2 a_0^3 [42] from the Sum-rule (magenta) agrees with B3LYP/6-31G(d) level (yellow) and MP2/6-31G* (light blue) at distance from 4\AA .

Likewise, figure B.2 presents $U(L)$ energies of $\text{Al} - \text{Al}^+$ atoms computed using quantum-chemical and the classical approach. The calculations for this

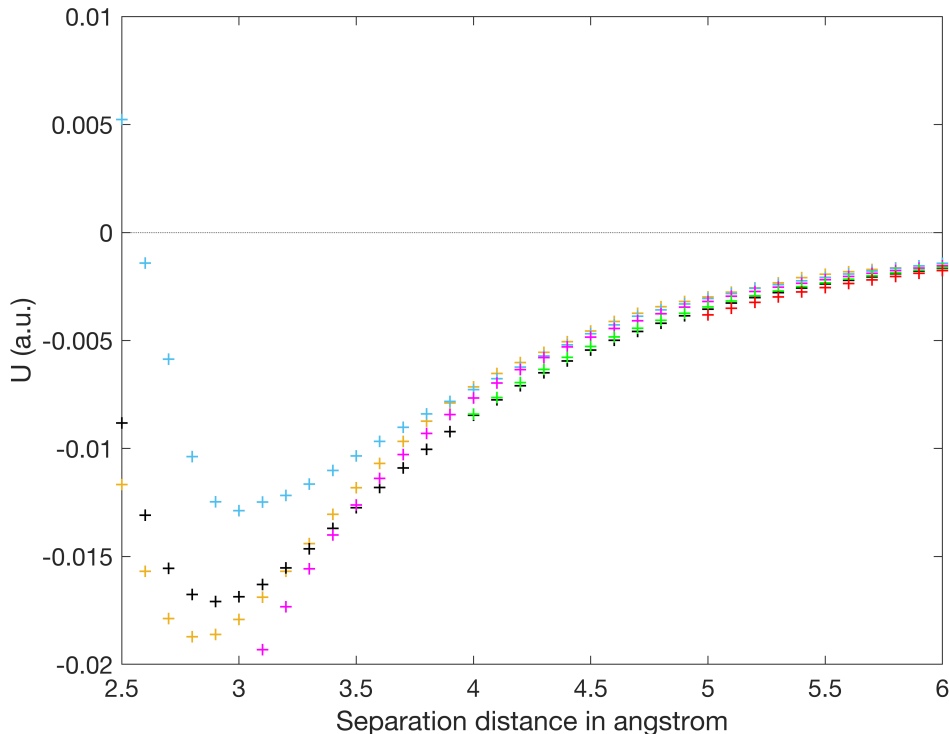


Figure B.1: *The polarisation portion of the interaction energy $U(L)$, in atomic units, for $\text{Al}^+ - \text{Al}^+$. The calculations are done with the CCSD(T)/aug-cc-pVTZ with no frozen core orbitals method (black), the density functional theory at the B3LYP/6-31G(d) level (yellow), MP2/6-31G* (light blue) For the rigorous classical formalism for two dielectric spheres three choices of parameters: $k_p = 3.52$, $a_1 = a_2 = 2\text{\AA}$ (green); $k_p = 154.96$, $a_1 = a_2 = 1.54\text{\AA}$ (magenta); $k_p = 1.915$, $a_1 = a_2 = 2.49\text{\AA}$ (red).*

comparison were carried out using also CCSD(T)/aug-cc-pVTZ, B3LYP/6-31G(d) and MP2/6-31G* level of theory and classical approach (described in section 2.3). The results of ion-neutral atom pair obtained using classical method for dielectric particles' radii of $a_{\text{Al}^+} = 2.48\text{\AA}$ for $24.4 a_0^3$ [41] and $a_{\text{Al}} = 5.05\text{\AA}$ for ground state a_0 from CCSDT equal to 57.74 [42] and $k_p = 1.93$ (red) overlaps with the results generated by CCSD(T)/aug-cc-pVTZ method. A system with smaller dielectric spheres of radii $a_{\text{Al}^+} = 2\text{\AA}$ for $24.65 a_0^3$ [41] and $a_{\text{Al}} = 4.07\text{\AA}$ for $a_0 = 57.74$ from CCSDT [42] and $k_p = 3.49$ (dark blue) very closely agrees to values calculated by using MP2/6-31G* (light blue).

Understanding the properties of systems at the molecular level is crucial such as metal pairs incorporated in catalysts' structures [47] and ion-pair residing in proteins [9, 48]. Regrettably, using expressions presented by Obolensky et

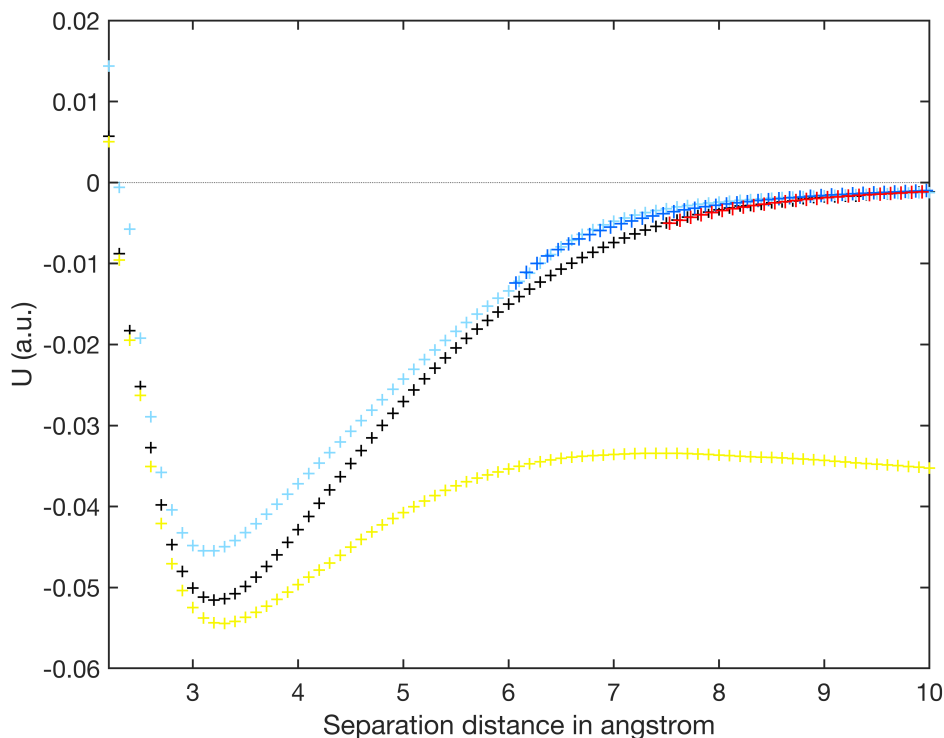


Figure B.2: The polarisation portion of the interaction energy $U(L)$, in atomic units, for $\text{Al} - \text{Al}^+$. The calculations are done with the $\text{CCSD(T)}/\text{aug-cc-pVTZ}$ with no frozen core orbitals method (black), the density functional theory at the $\text{B3LYP}/6\text{-}31\text{G}(\text{d},\text{p})$ level (yellow), $\text{MP2}/6\text{-}31\text{G}^*$ (light blue) For the rigorous classical formalism for two dielectric spheres two choices of parameters: $k_p = 3.49$, $a_{\text{Al}^+} = 2\text{\AA}$, $a_{\text{Al}} = 4.07\text{\AA}$ (dark blue); $k_p = 1.93$, $a_{\text{Al}^+} = 2.48\text{\AA}$, $a_{\text{Al}} = 5.05$ (red).

al.[41] did not give satisfying values at short separation distances for systems containing other metals when using the model of dielectric spheres applied in this research. Presented work manifests that classical methods could solve systems at a more efficient pace with quantum calculations' accuracy.

The work in Appendix B demonstrated the ability to calculate atomic-scale small systems by applying polarisable dielectric particles. The existing method only allows for the particles to come together at a touching point. The mentioned above overlapping method would also allow the particles to interact at even shorter distances, similarly to the quantum-mechanical methods. Also, developing more suitable formalism would enable the calculation of other atom and ions pairs and even more complex systems. This approach would significantly reduce the computational time.